c5cy00331h

12 AUTHORS, INCLUDING:

Maria Tereza Fabbro
Universitat Jaume I
8 PUBLICATIONS   17 CITATIONS

SEE PROFILE

Lourdes Gracia
Universitat Jaume I
61 PUBLICATIONS   845 CITATIONS

SEE PROFILE

Elson Longo
São Paulo State University
376 PUBLICATIONS   3,206 CITATIONS

SEE PROFILE

Laécio Santos Cavalcante
Universidade Estadual do Piauí (UESPI)
138 PUBLICATIONS   3,026 CITATIONS

SEE PROFILE

PAPER

CrossMark
click for updates

Facet-dependent photocatalytic and antibacterial properties of α-Ag₂WO₄ crystals: combining experimental data and theoretical insights†‡

R. A. Roca,[a] J. C. Sczancoski,[b] I. C. Nogueira,[c] M. T. Fabbro,[ac] H. C. Alves,[d] L. Gracia,[e] L. P. S. Santos,[c] C. P. de Sousa,[d] J. Andrés,[e] G. E. Luz Jr.,[f] E. Longo[b] and L. S. Cavalcante*[f]

In this paper, we have combined the various experimental results and first-principles calculations with a new and interesting discussion to explain the photocatalytic and antibacterial activities of α-Ag₂WO₄ crystals, which were obtained using the microwave-hydrothermal (MH) method with anionic surfactants. The advantages of the insights gained through the present work are two-fold. First, the mechanism and origin of the photocatalytic and antibacterial activities can be rationalized. Second, this facile and controllable synthetic method is expected to encourage the synthesis of complex metal oxides with specific active facets, and these insights can contribute to the rational design of new materials for multifunctional applications. X-ray diffraction and Rietveld refinement analysis confirmed that all the crystals have an orthorhombic structure without deleterious phases. Ultraviolet–visible diffuse reflectance spectroscopy indicated the presence of intermediary energy levels and a variation in the optical band gap values (3.09–3.14 eV) with the crystal growth process. The geometry, electronic properties of the bulk, and surface energies of these crystals were evaluated using first-principles quantum mechanical calculations based on the density functional theory. The crystal shapes was experimentally and theoretically modeled based on Rietveld refinement data, emission scanning electron microscopy images, and Wulff construction. To obtain a wide variety of crystal shapes, the morphologies were gradually varied by tuning the surface chemistry, i.e., the relative stability of the faceted crystals. The growth mechanisms of different α-Ag₂WO₄ crystals and their facet-dependent photocatalytic and antibacterial performances were explored in details. The combination of experimental and theoretical data revealed the presence of (110) and (011) planes with high surface energies together with the disappearance of faces related to the (010)/(01̄0) planes in α-Ag₂WO₄ crystals are key factors that can rationalize both the photocatalytic and antibacterial activities. The different activities may be attributed to the different number of unsaturated superficial Ag and W atoms capable of forming the main active adsorption sites. Finally, we discuss how knowledge of surface-specific properties can be utilized to design a number of crystal morphologies that may offer improved performance in various applications.

1. Introduction

Silver tungstate (Ag₂WO₄) is an important multifunctional material with an orthorhombic structure that exhibits various physical and chemical properties such as photoluminescence,[1–6] photocatalysis,[7–9] ozone gas sensing,[10] and antibacterial activity against Gram-negative and Gram-positive bacterial strains, for example, *Escherichia coli*, *Bacillus subtilis*,

[a] DQ-Universidade Federal de São Carlos, P.O. Box 676, 13565-905 São Carlos, São Paulo, Brazil

[b] CDMF-Universidade Estadual Paulista, P.O. Box 355, 14801-907, Araraquara, SP, Brazil

[c] Instituto Federal do Maranhão, Química e PPG em Engenharia de Materiais, 65025-001, 65030-005, São Luís, MA, Brazil

[d] Programa de Pós-Graduação em Biotecnologia, P.O. Box 676, 13565-905, São Carlos, SP, Brazil

[e] Departamento de Química Física y Analítica, Universitat Jaume I (UJI), Castelló 12071, Spain

[f] PPGQ-GERATEC-CCN-DQ, Universidade Estadual do Piauí, João Cabral, N. 2231, P.O. Box 381, 64002-150 Teresina, PI, Brazil. E-mail: laeciosc@gmail.com

methicillin-resistant *Staphylococcus aureus* (MRSA), or simply *Staphylococcus aureus*.[11,12] Moreover, this material acts as a bifunctional catalyst in the chemical fixation of carbon dioxide (CO_2) to produce α-alkylidene cyclic carbonates, α-alkylidene cyclic carbamates, and β-oxopropylcarbamates[13] and as a single-component bifunctional catalyst for the carboxylation of terminal alkynes with CO_2 under ambient conditions,[14] exhibits electrocatalytic activity for the reduction of *p*-nitrophenol, K_2CrO_4, and H_2O_2 in basic solution[15] as well as for the detection of catechol,[16] and has the ability to absorb halogen- and sulfur-containing products.[17]

Ag_2WO_4 crystals can have three crystal structure types. These three polymorphs are assigned as alpha (α) for the orthorhombic structure with space group $Pn2n$, beta (β) for the hexagonal structure with space group $P6_3/m$, and gamma (γ) for the cubic structure with space group $Fd\bar{3}m$.[18] Among the electronic structures mentioned above, heterogeneous photocatalysis using α- or β-Ag_2WO_4 crystals as catalyst has shown significant potential for the treatment of polluted water with different organic/textile dyes or aromatic organic compounds, such as methyl blue,[7] Rhodamine B,[7–9], methyl orange, phenol,[19,20] reactive orange 86, and reactive brilliant red.[20] Basically, photocatalysis is a physical–chemical process based on the acceleration of a photoreaction in the presence of a semiconductor catalyst.[21] This process has been explained as the reduction and oxidation of chemical species in organic dyes by electron–hole pairs, which are generated between the valence band (VB) and the conduction band (CB) of the catalyst, following the absorption of ultraviolet light or sunlight.[21–23] Moreover, the α- or β-Ag_2WO_4 crystals have been shown to be highly capable of killing Gram-negative (*E. coli*), Gram-positive (MRSA or *S. aureus*), or DH 5α bacteria both on surfaces and in solution.[11,12,24,25] Among these bacteria, *E. coli* is facultative anaerobic bacteria, which are more likely to survive in acidic environments; therefore, a continuous alkaline environment in a glaze layer is more conducive to antibiosis.[26] *E. coli* is one of the few live microorganisms on Earth that are capable of producing all components found in basic organic compounds.[27] The presence of *E. coli* in H_2O or food is indicative of contamination with human or animal feces. Contamination is very common and easily spreads in H_2O, which can contaminate food when it comes in contact, thereby promoting congenital transmission of *E. coli* bacteria.[28–30] Thus, several researchers around the world have investigated different inorganic antibacterial agents[31–35] to combat these microorganisms that spread easily, are difficult to control, and exist in almost all parts of the planet and in many foods we eat. Among the various inorganic materials, silver has been employed most extensively since ancient times to fight infections and control spoilage. The antibacterial and antiviral actions of silver, silver ions, and silver compounds have been thoroughly investigated,[36,37] and in minute concentrations, silver is nontoxic to human cells.[38] In particular, among the well-known silver nanoparticles, compounds based on silver molybdate have presented excellent antibacterial properties.[38]

In general, photocatalytic and antibacterial reactions occur at the interface, and photocatalysis requires the effective adsorption of reactant molecules or ions on the surface of Ag_2WO_4 crystals. The adsorption states of some specific molecules or ions are intrinsically determined by the surface atomic structures of Ag_2WO_4. Therefore, their performance is strongly associated with the electronic and surface structure, as well as the morphology. Moreover, a discussion of the discrepancies among surface atomic structures with different facet depths is highly significant, because a better understanding of the reason for facet-dependent photocatalytic and antibacterial activities is necessary to prepare materials with enhanced properties. First-principles theoretical calculations, mainly within the framework of density functional theory (DFT), have proved invaluable in providing guidance and atomistic understanding of Ag_2WO_4 crystals.
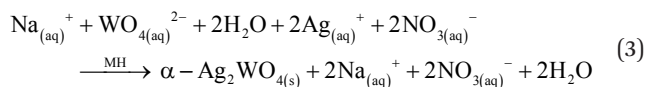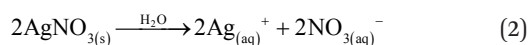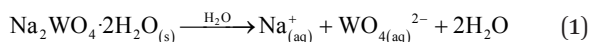
Therefore, in this article, we clarify these issues by performing a detailed theoretical and experimental study on the photocatalytic (PC) and antibacterial (AB) activities of α-Ag_2WO_4 crystals. Herein, we present a microwave-hydrothermal (MH) method to synthesize shape-controlled α-Ag_2WO_4 crystals without the necessity of seed crystals, environmentally harmful chemicals, or severe reaction conditions. Moreover, these microcrystals were characterized using X-ray diffraction (XRD) and Rietveld refinement data, and their optical band gaps were obtained by ultraviolet–visible (UV–vis) diffuse reflectance spectroscopy measurements. Field emission scanning electron microscopy (FE-SEM) images were employed to monitor the evolution of shape, average size, and growth process of the crystals with increasing MH processing temperature. The PC activity for the degradation of Rhodamine B after 120 min and Rhodamine 6G after 100 min under UV light were discussed in details. To complement the experimental data, we carried out first-principles calculations to build various crystal shapes that are associated with the relative surface energy values for each face. We combined first-principles calculations with an algorithm based on Wulff construction to find suitable crystals with a specific shape. Finally, the AB activity for the inactivation of *E. coli* bacteria was explained. The insights gained through these calculations have two advantages: they help rationalize the mechanism and origin of the photocatalytic and antibacterial activities, and they can contribute to the rational design of new materials for multifunctional applications.

2. Experimental and theoretical methodology

2.1. MH synthesis of α-Ag_2WO_4 microcrystals

α-Ag_2WO_4 crystals were prepared by the MH method at different temperatures (100, 120, 140, and 160 °C) for 1 h with the anionic surfactant sodium dodecyl sulfate (SDS, $C_{12}H_{25}SO_4Na$; 99%, Sigma-Aldrich). The typical synthesis procedure is described as follows: 1×10^{-3} mol of tungstate sodium dihydrate ($Na_2WO_4 \cdot 2H_2O$; 99.5%, Sigma-Aldrich) and 2×10^{-3} mol of silver nitrate ($AgNO_3$; 99.8%, Sigma-

Aldrich) were separately dissolved in 50 mL of deionized water contained in plastic tubes (Falcon) in which 1 g of SDS had previously been dissolved. These suspensions were transferred into a Teflon-lined vessel autoclave without stirring, which was then sealed and placed in an adapted domestic microwave system (NN-ST357WRPH Piccolo 22 L, Panasonic) and processed at different temperatures for 1 h. The temperature of the system was monitored using an in-vessel temperature sensor (CNT-120, Incon Electronic Ltda, São Carlos, SP, Brazil). The MH reactions were carried out in 150 mL polyethylene vessels. The α-Ag$_2$WO$_4$ crystals were obtained as a light beige colored, finely powdered precipitate. The reaction between $(2Ag^+ \leftarrow \ :WO_4{}^{2-})$ ions resulted in the formation of crystalline α-Ag$_2$WO$_4$ precipitates, as shown in eqn (1)–(3) below:

$$Na_2WO_4 \cdot 2H_2O_{(s)} \xrightarrow{\ H_2O\ } Na^+_{(aq)} + WO_4{}^{2-}_{(aq)} + 2H_2O \quad (1)$$

$$2AgNO_{3(s)} \xrightarrow{\ H_2O\ } 2Ag^+_{(aq)} + 2NO_3{}^-_{(aq)} \quad (2)$$

$$Na^+_{(aq)} + WO_4{}^{2-}_{(aq)} + 2H_2O + 2Ag^+_{(aq)} + 2NO_3{}^-_{(aq)}$$
$$\xrightarrow{\ MH\ } \alpha - Ag_2WO_{4(s)} + 2Na^+_{(aq)} + 2NO_3{}^-_{(aq)} + 2H_2O \quad (3)$$

The resulting suspensions were washed with deionized water several times to remove the Na$^+$, NO$_3{}^-$ or SO$_4{}^{2-}$ ions and organic compounds residuals. Finally, the precipitate was collected and dried with acetone at room temperature for 6 h.

2.2. Structural characterization of α-Ag$_2$WO$_4$ microcrystals

The α-Ag$_2$WO$_4$ crystals were structurally characterized by XRD using a D/Max-2500PC diffractometer (Rigaku, Japan) with Cu-Kα radiation (λ = 1.5406 Å) in the 2θ range from 5° to 75° with a scanning velocity of 2° min^{-1} in the normal routine and from 10° to 110° with a scanning velocity of 1° min^{-1} in the Rietveld routine. UV–vis diffuse reflectance measurements were obtained using a Cary 5G spectrophotometer (Varian, USA) in diffuse reflection mode. The shapes and sizes of the α-Ag$_2$WO$_4$ microcrystals were observed using a field-emission scanning electron microscope operated at 20 kV (Inspect F50, FEI Company, Hillsboro, USA) and at 10 kV (Supra 35-VP, Carl Zeiss, Germany). The specific surface area was recorded on an ASAP 2000 Phys/Chemisorption unit (Micromeritics, USA). In addition, the Brunauer–Emmett–Teller (BET) method was employed to estimate the specific surface area of the crystals.

2.3. Photocatalytic activity measurements of α-Ag$_2$WO$_4$ microcrystals

PC properties of these crystals (as a catalyst) for the degradation of [9-(2-carboxyphenyl)-6-diethylamino-3-xanthenylidene]-diethylammonium chloride, which is known as tetraethylated Rhodamine or Rhodamine B (RhB; 95%,

Mallinckrodt), and Rhodamine 6G (Rh6G, C$_{28}$H$_{31}$ClN$_2$O$_3$; 95%, Sigma-Aldrich) in aqueous solution were tested under UV light. Crystals of the catalyst (30 mg) were placed in 250 mL beakers, and 50 mL of an RhB or Rh6G solution (1 × 10^{-5} mol L^{-1}, pH = 4) was added. The suspensions were ultrasonicated for 5 min in an ultrasonic cleaner (Model 1510, Branson) with a frequency of 42 kHz before illumination and then stored in the dark for 5 min to allow the saturated absorption of RhB or Rh6G onto the catalyst. The beakers were then placed in a photo-reactor at 20 °C and illuminated by six UV lamps (TUV Phillips, 15 W, and maximum intensity at 254 nm). At ten-minute intervals, a 3 mL aliquot was removed and centrifuged at 9000 rpm for 10 min to remove the crystals from the suspension. Finally, variations in the absorption band maximum of the supernatant solutions were monitored by UV–vis spectroscopy using a double-beam spectrophotometer with a double monochromator and a photomultiplier tube detector (JASCO V-660, USA).

2.4. Antibacterial activity measurement of α-Ag$_2$WO$_4$ microcrystals

To determine the AB activity of α-Ag$_2$WO$_4$ microcrystals against Gram-negative bacterial colonies, *E. coli* was used in saturated aqueous suspensions (1 mg mL^{-1}) of these crystals. The culture media used in the biological tests were approximately 1 × 10^8 colony forming units per milliliter (CFU mL^{-1}), which was determined by comparing with a McFarland solution using a UV–vis spectrophotometer at 325 nm. A series of decimal dilutions were carried out and used bioassays of 24 h duration with an initial *E. coli* bacteria population of around 1 × 10^3 CFU mL^{-1} (stirring at 120 rpm, incubation temperature of 35 °C). The experiments were performed in screw cap test tubes containing the liquid culture medium; the bacterial concentrations of the inoculums tested were 0.1–10 mg mL^{-1} for four types of α-Ag$_2$WO$_4$ microcrystals obtained by the MH method at 100, 120, 140, and 160 °C. Each tube had a final volume of 10 mL. All analyses were performed in triplicate, including the control group, which only contained the culture medium, and the control where only anionic surfactants (SDS) were added to show the surfactant has not influence on the results of the crystals. After this step, the surfactants were completely removed from the crystals before the washing process and the utilization in biological medium.

2.5. Theoretical procedure and computational method

First-principles total-energy calculations were carried out within the periodic DFT framework using the VASP program.[39–41] The Kohn–Sham equations were solved using the generalized gradient approximation (GGA) in the Perdew–Burke–Ernzerhof (PBE) formulation for the electron exchange and correlation contribution to the total energy.[41,42] The conjugated gradient energy minimization method was used to obtain relaxed systems by requiring the forces experienced by each atom to be smaller than 0.01 eV Å^{-1}. The electron–ion

interaction was described by the projector-augmented-wave pseudopotentials. The plane-wave expansion was truncated at a cut-off energy of 460 eV, and the Brillouin zones were sampled through the Monkhorst–Pack special k-point grid to ensure geometrical and energetic convergence for the α-Ag$_2$WO$_4$ crystal surfaces.[43,44]

To confirm the convergence of the total energy with respect to the slab thickness of the different surface models, the surface energy (E_{surf}) for several low-index planes was calculated. E_{surf} is defined as the total energy per repeating cell of the slab minus the total energy for the same number of atoms in the perfect crystal and then divided by the surface area per repeating cell for the two sides of the slab, as shown in eqn (4):

$$E_{surf} = \frac{\left(E_{slab} - nE_{bulk}\right)}{2A} \quad (4)$$

From the thermodynamic point of view, the equilibrium shape of a crystal is determined by the free energies of various facets, E_{surf}, and can be calculated using a classic Wulff construction that minimizes the total surface free energy at a fixed volume.[45] The Wulff theorem[46] provides a simple relation between the E_{surf} of each (hkl) plane and its distance (d) in the normal direction from the center of the crystallite.

Several insightful review papers have reported experimental and theoretical calculation studies on the important aspects that govern crystal shape modulation in semiconductors.[47–50] In this context, our research group has developed a working methodology to study the morphology of different metal oxides such as SnO$_2$,[51] PbMoO$_4$,[52] and CaWO$_4$.[53]

3. Results and discussion

3.1. X-ray diffraction analysis

Fig. 1a–d show the XRD patterns of α-Ag$_2$WO$_4$ crystals synthesized by the MH method for 1 h with 1 g of SDS at different temperatures.

In Fig. 1, XRD patterns indicate that all α-Ag$_2$WO$_4$ crystals have an orthorhombic structure without any deleterious phases and with the space group $Pn2n$ and point-group symmetry (C_{2v}^{10}).[54] These crystals have sharp and well-defined diffraction peaks, which indicate a good degree of structural order and crystallinity at long range in the lattice. However, it is difficult to verify the existence of Ag nanoparticles in the lattice of these crystals from the XRD measurements.[55] Moreover, all diffraction peaks are in good agreement with the respective Inorganic Crystal Structure Database (ICSD) no. 4165 and the literature.[54,56]

3.2. Rietveld refinement analysis

The Rietveld method is based on the construction of diffraction patterns calculated according to the structural model.[57] The calculated patterns are adjusted to fit the observed patterns and thus provide the structural parameters of the
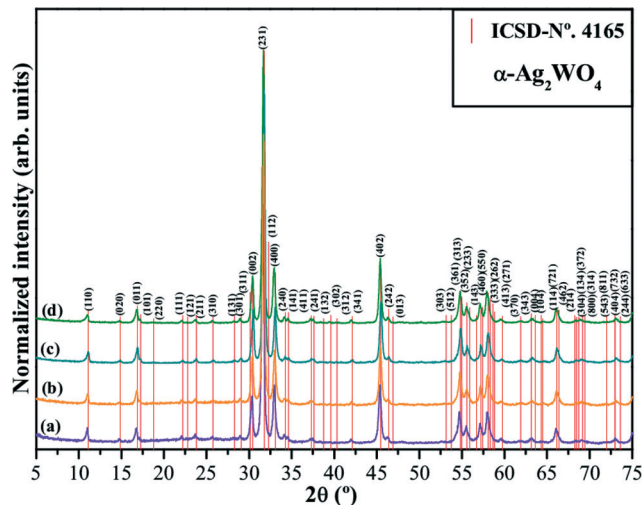

Fig. 1 XRD patterns of α-Ag$_2$WO$_4$ microcrystals synthesized by the MH method at different temperatures: (a) 100, (b) 120, (c) 140, and (d) 160 °C. The vertical lines (|) indicate the respective positions and intensities found in ICSD card no. 4165 corresponding to the α-Ag$_2$WO$_4$ phase.

material and the diffraction profile. In this work, the Rietveld method was applied to adjust the atomic positions, lattice parameters, and unit cell volume. The Rietveld refinement was performed using the general structure analysis (GSAS) program.[58] In these analyses, the refined parameters were the scale factor, background, shift lattice constants, profile half-width parameters (u, v, w), isotropic thermal parameters, lattice parameters, strain anisotropy factor, preferential orientation, and atomic functional positions. The background was corrected using a Chebyschev polynomial of the first kind. The peak profile function was modeled using a convolution of the Thompson–Cox–Hastings pseudo-Voigt (pV-TCH) function[59] with the asymmetry function described by Finger et al.,[60] which accounts for the asymmetry due to axial divergence. To account for the anisotropy in the half width of the reflections, the model by Stephens[61] was used.

Fig. 2a–d show the Rietveld refinement plots for the α-Ag$_2$WO$_4$ crystals synthesized by the MH method.

All structural refinement results obtained using the Rietveld method[57] were quite consistent with ICSD no. 4165 reported by Skarstad and Geller.[54] However, the lower angle region where the most intense peaks are located revealed a major difference. An increase in the differences in this region can be related to the characteristics of the pattern with narrow peaks and high intensities. According to the literature,[18] Ag$_2$WO$_4$ crystals can exhibit polymorphisms because this oxide has three structure types depending on the pH range (acid or alkaline): α-orthorhombic with the space group $Pn2n$, β-hexagonal with the space group $P6_3/m$, and γ-cubic with the space group $Fd\bar{3}m$. In this study, all crystals were prepared at pH value of 6. Therefore, the structural refinement method was performed to confirm the orthorhombic
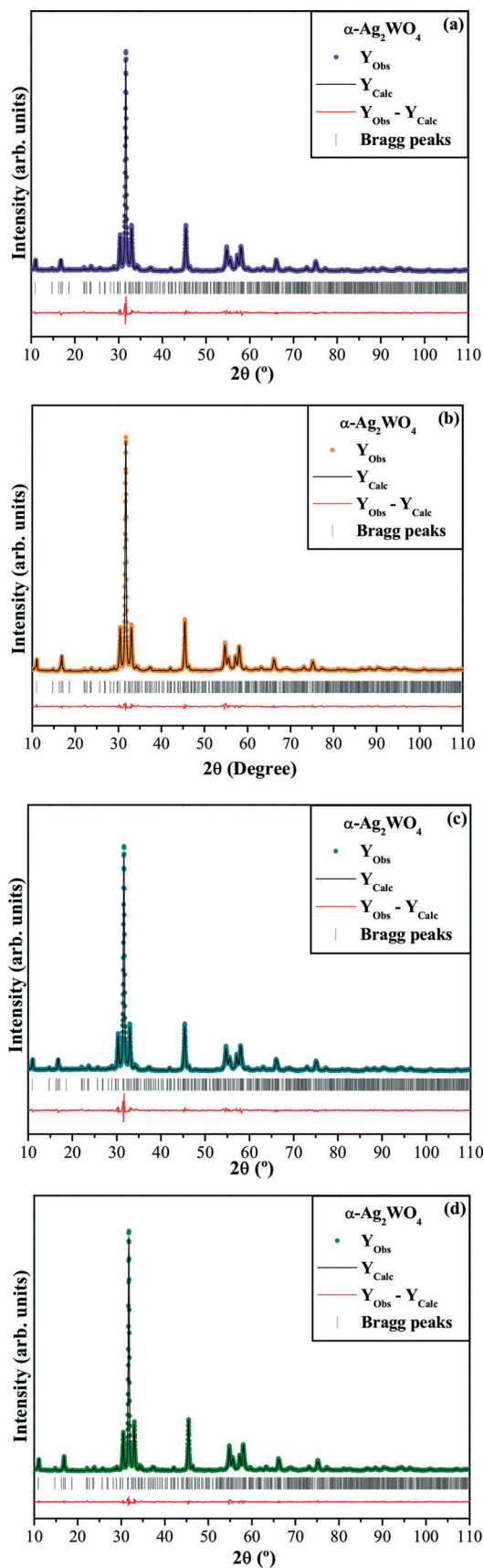
Fig. 2 Rietveld refinement plots of α-Ag$_2$WO$_4$ microcrystals synthesized by the MH method at different temperatures: (a) 100, (b) 120, (c) 140, and (d) 160 °C.

structure of α-Ag$_2$WO$_4$ crystals. The quality of the structural refinement is generally checked using R-values (R_{wp}, R_{Bragg}, R_p, χ^2, and S); these values are easy to determine and are consistent with an orthorhombic structure. However, in general, experimentally observed XRD patterns and theoretically calculated data display small differences near zero on the intensity scale, as illustrated by the line $Y_{Obs} - Y_{Calc}$. More details regarding the Rietveld refinement are displayed in Table 1a–d.

In this table, the statistical parameters (R_{wp}, R_{Bragg}, R_p, χ^2, and S) show small deviations, which indicate the good quality of the structural refinement and numerical results. The structural refinement data confirmed all α-Ag$_2$WO$_4$ crystals were crystallized in an orthorhombic structure with space group $Pn2n$, point-group symmetry (C_{2v}^{10}) and two molecular formula units per unit cell ($Z = 2$).[54] However, some variations in the atomic positions of silver, tungsten, and oxygen atoms were observed because the atoms do not occupy fixed positions in this specific type of structure. These results indicate major variations in the position of oxygen atoms owing to significant lattice distortions, as shown by XRD. Therefore, we believe that these major variations in the atomic positions of the oxygen atoms can lead to the formation of different types of distortions in the Ag–O or W–O bonds leading to formation of distorted clusters, such as [AgO$_y$] (y = 7, 6, 4, and 2) and [WO$_6$] clusters over the long range in this specific type of crystalline lattice.

3.3. Unit cell representation and the symmetry, geometry, and coordination of the clusters in α-Ag$_2$WO$_4$ crystals

Fig. 3a and b show a schematic representation of orthorhombic α-Ag$_2$WO$_4$ unit cells and the symmetry, geometry, and coordination of each cluster modeled from the Rietveld refinement data, respectively.

The unit cell shown in Fig. 3(a) was modeled through the visualization system for electronic and structural analysis (VESTA) program (version 3.2.1 for Windows)[62,63] using the lattice parameters and atomic positions obtained from the Rietveld refinement data presented in Table 1a–d. Moreover, Fig. 3(a) shows that the O–Ag–O and O–W–O bonds are projected out of the unit cell. In these unit cells, all W (W1, W2, and W3) atoms are coordinated to only six O atoms, thus forming distorted octahedral [WO$_6$] clusters in the lattice with the symmetry group O_h (Fig. 3b). The differences in O–W–O bond lengths and angles can lead to different degrees of distortion or intrinsic order–disorder in this type of lattice. In addition, Ag atoms in these unit cells can exhibit four types of cluster coordination. The Ag1 and Ag2 atoms are coordinated to seven O atoms, forming distorted deltahedral [AgO$_7$] clusters, which are irregular pentagonal dipyramid polyhedra with symmetry group D_{5h} (Fig. 3b). The Ag3 atoms are bonded to six O atoms, which form distorted octahedral [AgO$_6$] clusters with symmetry group O_h (Fig. 3b). The Ag4 and Ag5 atoms are coordinated to four O atoms, forming distorted tetrahedral [AgO$_4$] clusters with

Table 1 Rietveld refinement results for α-Ag₂WO₄ crystals obtained at different temperatures: (a) 100 °C, (b) 120 °C, (c) 140 °C and (d) 160 °C for 1 h with 1 g of SDS by the MH method

(a)

Atom	Wyckoff	Site	x	y	z
W1	4c	1	0.25409	0	0.52544
W2	2b	2	0	0.84751	0.5
W3	2b	2	0	0.138	0.5
Ag1	4c	1	0.751	0.1711	0.9879
Ag2	4c	1	0.2348	0.8176	0.0091
Ag3	2a	2	0	0.9872	0
Ag4	2a	2	0	0.65315	0
Ag5	2a	2	0	0.3147	0
Ag6	2b	2	0	0.5093	0.5
O1	4c	1	0.36737	0.6120	0.1956
O2	4c	1	0.3678	0.3780	0.1888
O3	4c	1	0.4195	0.73502	0.814
O4	4c	1	0.4248	0.263	0.7913
O5	4c	1	0.16252	0.494	0.2821
O6	4c	1	0.4134	0.496	0.8456
O7	4c	1	0.189	0.612	0.8561
O8	4c	1	0.1927	0.3791	0.8984

a = 10.875(1) Å, b = 12.017(6) Å, c = 5.898(4) Å; V = 770.88(1) Å³; Z = 2; R_{wp} = 8.25%; R_{Bragg} = 3.62%; R_p = 6.56%; χ^2 = 2.77 and S = 1.66

(b)

Atom	Wyckoff	Site	x	y	z
W1	4c	1	0.2541	0	0.5253
W2	2b	2	0	0.84746	0.5
W3	2b	2	0	0.138	0.5
Ag1	4c	1	0.7511	0.1711	0.9878
Ag2	4c	1	0.235	0.8176	0.0095
Ag3	2a	2	0	0.9874	0
Ag4	2a	2	0	0.6532	0
Ag5	2a	2	0	0.3147	0
Ag6	2b	2	0	0.5093	0.5
O1	4c	1	0.3671	0.612	0.1951
O2	4c	1	0.3672	0.3781	0.1886
O3	4c	1	0.4203	0.7351	0.8148
O4	4c	1	0.4243	0.263	0.7921
O5	4c	1	0.1631	0.494	0.2806
O6	4c	1	0.4127	0.496	0.8455
O7	4c	1	0.1888	0.612	0.8571
O8	4c	1	0.193	0.3792	0.8973

a = 10.873(8) Å, b = 12.010(5) Å, c = 5.8939(5) Å; V = 769.75(5) Å³; Z = 2; R_{wp} = 7.8%; R_{Bragg} = 3.64%; R_p = 5.71%; χ^2 = 2.71 and S = 1.64

(c)

Atom	Wyckoff	Site	x	y	z
W1	4c	1	0.2554	0	0.5251
W2	2b	2	0	0.8472	0.5
W3	2b	2	0	0.1392	0.5
Ag1	4c	1	0.7514	0.1706	0.9867
Ag2	4c	1	0.2354	0.8167	0.0095
Ag3	2a	2	0	0.9884	0
Ag4	2a	2	0	0.6564	0
Ag5	2a	2	0	0.3149	0
Ag6	2b	2	0	0.5101	0.5
O1	4c	1	0.3655	0.6141	0.1987
O2	4c	1	0.3741	0.3772	0.1945
O3	4c	1	0.4252	0.7386	0.7892
O4	4c	1	0.3982	0.2843	0.8012
O5	4c	1	0.1705	0.4879	0.2915
O6	4c	1	0.4125	0.4894	0.8672
O7	4c	1	0.1978	0.6215	0.8791
O8	4c	1	0.1987	0.3881	0.8788

a = 10.884(1) Å, b = 12.014(8) Å, c = 5.8953(5) Å; V = 770.93(1) Å³; Z = 2; R_{wp} = 8.99%; R_{Bragg} = 3.03%; R_p = 7.14%; χ^2 = 3.46 and S = 1.86

Table 1 (continued)

(d)

Atom	Wyckoff	Site	x	y	z
W1	4c	1	0.254	0	0.5254
W2	2b	2	0	0.8475	0.5
W3	2b	2	0	0.138	0.5
Ag1	4c	1	0.751	0.1711	0.9878
Ag2	4c	1	0.235	0.8177	0.0093
Ag3	2a	2	0	0.9873	0
Ag4	2a	2	0	0.6532	0
Ag5	2a	2	0	0.3148	0
Ag6	2b	2	0	0.5092	0.5
O1	4c	1	0.3678	0.612	0.1945
O2	4c	1	0.3684	0.3781	0.1875
O3	4c	1	0.4196	0.735	0.8152
O4	4c	1	0.4251	0.2631	0.7924
O5	4c	1	0.1624	0.4941	0.2813
O6	4c	1	0.4136	0.496	0.8468
O7	4c	1	0.1891	0.612	0.8564
O8	4c	1	0.1931	0.3883	0.899

a = 10.891(3) Å, b = 12.011(2) Å, c = 5.890(4) Å; V = 770.56(7) Å³; Z = 2; R_{wp} = 7.8%; R_{Bragg} = 3.64%; R_p = 5.71%; χ^2 = 2.71 and S = 1.64

symmetry group T_d. Moreover, we verify that the Ag4 atoms form distorted tetrahedral [AgO₄] clusters more often than the Ag5 atoms (Fig. 3b), whereas the Ag6 atoms bond to two O atoms to form angular [AgO₂] clusters with the symmetry group C_{2v} and an O–Ag–O bond angle of 170.5°.

3.4. UV–vis diffuse reflectance spectroscopy analyses

The optical band gap energy (E_{gap}) was calculated using the method proposed by Kubelka and Munk.[64] This methodology is based on the transformation of diffuse reflectance measurements to estimate E_{gap} values with good accuracy within the limits of the assumptions when modeled in three dimensions.[65] Particularly, it is useful in limited cases with an infinitely thick sample layer. The Kubelka–Munk eqn (5) for any wavelength is described as follows:

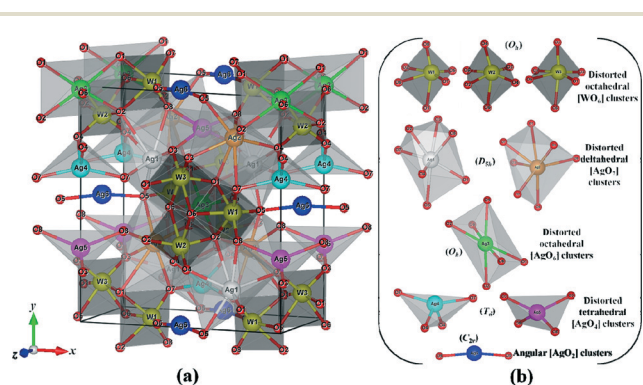$$F\left(R_\infty\right) \equiv \frac{\left(1-R_\infty\right)^2}{2R_\infty} = \frac{k}{s} \tag{5}$$

Fig. 3 (a) Schematic representation of the orthorhombic unit cells corresponding to α-Ag₂WO₄ crystals and (b) coordination polyhedra and symmetry for all the clusters.

where $F(R_\infty)$ is the Kubelka–Munk function or absolute reflectance of the sample. In our case, magnesium oxide (MgO) was the standard sample used in reflectance measurements. $R_\infty = R_{sample}/R_{MgO}$, where R_∞ is the reflectance when the sample is infinitely thick, k is the molar absorption coefficient, and s is the scattering coefficient. In a parabolic band structure, the optical band gap and absorption coefficient of the semiconductor oxides[66] can be calculated using the following eqn (6):

$$\alpha h\nu = C_1(h\nu - E_{gap})^n \qquad (6)$$

where α is the linear absorption coefficient of the material, $h\nu$ is the photon energy, C_1 is a proportionality constant, and n is a constant associated with the type of electronic transitions ($n = 0.5$, 2, 1.5, and 3 for direct allowed, indirect allowed, direct forbidden, and indirect forbidden transitions, respectively). According to Tang et al.[67] and Kim et al.,[68] silver tungstate crystals exhibit an optical absorption spectrum governed by direct electronic transitions between the VB and the CB. Moreover, our theoretical calculations obtained for the bulk α-Ag$_2$WO$_4$ crystals with an orthorhombic structure in the neutral state indicated a direct optical band gap. In this electronic process, after the electronic absorption process, the electrons located in the maximum-energy states in the VB return to the minimum-energy states in the CB at the same point in the Brillouin zone.[69] Based on this information, the E_{gap} values of our α-Ag$_2$WO$_4$ crystals were calculated using $n = 0.5$ in eqn (6). Finally, using the remission function described in eqn (5) with the term $k = 2\alpha$ and C_2 as a proportionality constant, we obtain the modified Kubelka–Munk equation, as indicated in eqn (7):

$$[F(R_\infty)h\nu]^2 = C_2(h\nu - E_{gap}) \qquad (7)$$

By finding the $F(R_\infty)$ value from eqn (7) and plotting $[F(R_\infty)h\nu]^2$ against $h\nu$, the E_{gap} value of the α-Ag$_2$WO$_4$ crystals was determined.

Fig. 4a–d show the UV–vis diffuse reflectance spectra for the α-Ag$_2$WO$_4$ crystals synthesized by the MH method.

As observed in Fig. 4a–d, E_{gap} values increase with increasing MH processing temperature. In principle, we believe this behavior is related to a decrease in the intermediary energy levels between the VB and the CB because the exponential optical absorption edge and the optical band gap energy are controlled by the degree of structural order–disorder in the lattice.[70] On the other hand, a decrease in the E_{gap} values can be attributed to the existence of medium-range structural defects, local bond distortions, intrinsic surface states, and interfaces, which yield localized electronic levels within the forbidden band gap.[70,71] For a simplified description, we attributed these differences in the E_{gap} values mainly to distortions of [AgO$_y$] (y = 7, 6, 4, and 2) and [WO$_6$] clusters over the short- and medium-ranges based on our theoretical calculations for α-Ag$_2$WO$_4$ crystals.[4]
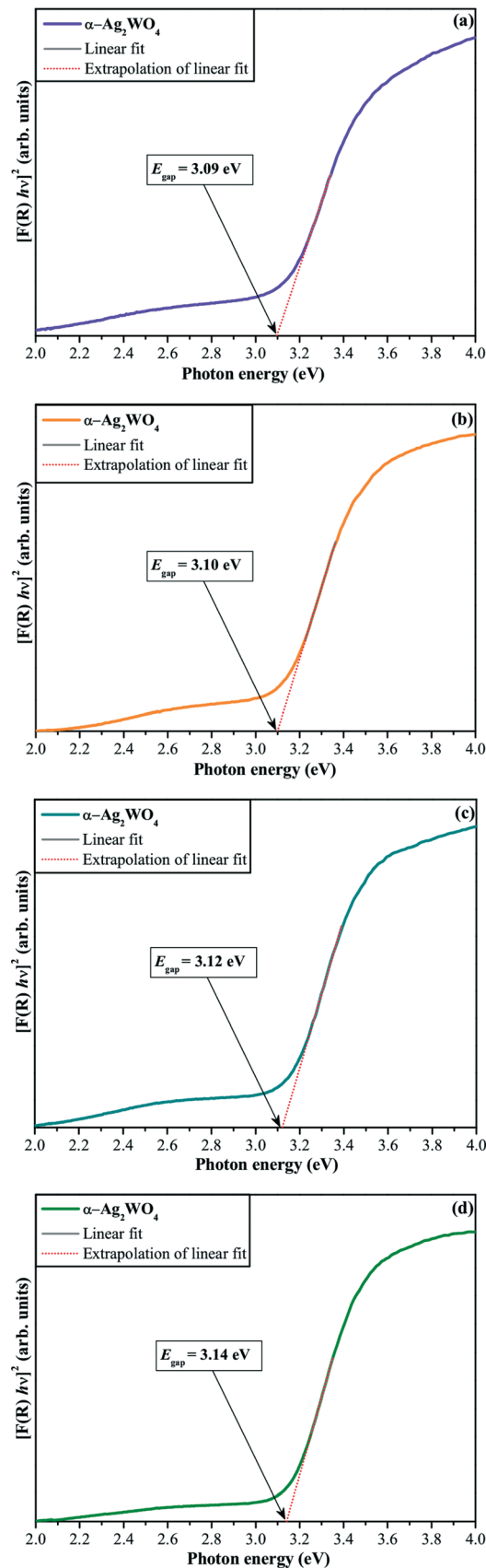

Fig. 4 UV–vis spectra of α-Ag$_2$WO$_4$ microcrystals synthesized by the MH method at different temperatures: (a) 100, (b) 120, (c) 140, and (d) 160 °C.
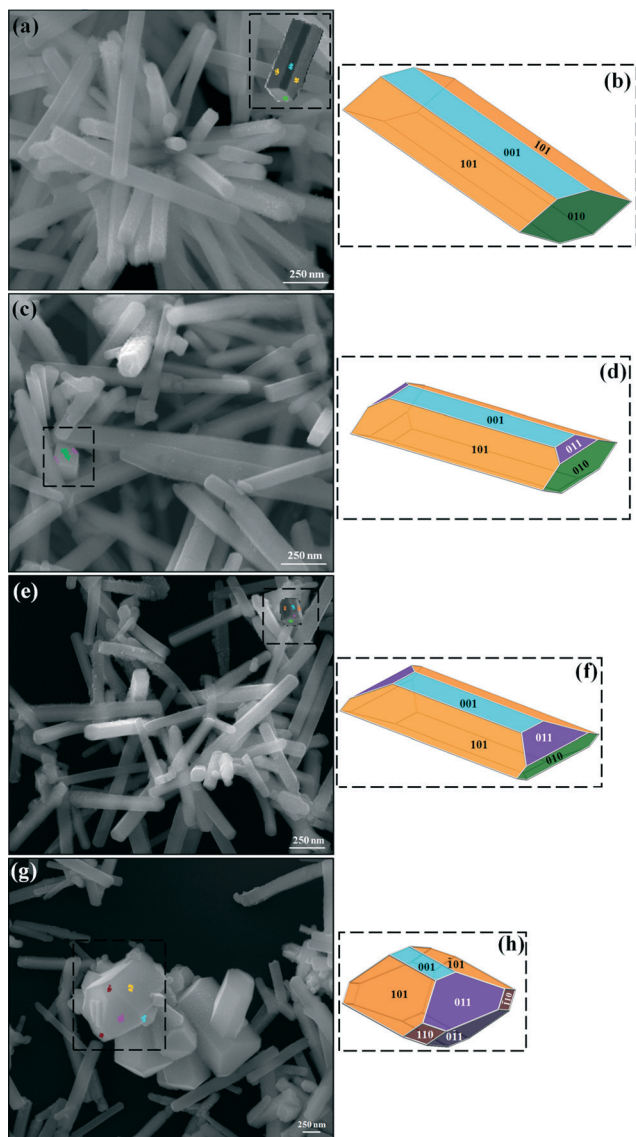
Fig. 5 FE-SEM images and crystal shape simulated computationally for α-Ag$_2$WO$_4$ microcrystals synthesized by the MH method at different temperatures: (a, b) 100, (c, d) 120, (e, f) 140, and (g, h) 160 °C, respectively.

3.5. FE-SEM image analyses

Fig. 5a, c, e, and g show the FEG-SEM images of α-Ag$_2$WO$_4$ crystals synthesized by the MH method and Fig. 5b, d, f, and h display single α-Ag$_2$WO$_4$ crystals, which were modeled computationally based on our Rietveld refinement data and FE-SEM images.

FEG-SEM images were of fundamental importance to understanding the evolution of the growth process and changes in the surfaces of the crystals with the variation in the MH processing temperature. In Fig. 5(a), a large quantity of α-Ag$_2$WO$_4$ crystals with 8 faces are observed, which were grown by MH at 100 °C for 1 h. These crystals have an agglomerate nature and a hexagonal rod-like shape elongated in y-axis along the [010] direction. Some Ag nanoparticles were grown on the surface of α-Ag$_2$WO$_4$ crystals owing to

the accelerated electron beam from the electronic microscope under high vacuum, which is a phenomenon that has already been elucidated and thoroughly discussed in our previous papers.[2–5] Inset in Fig. 5(a) clearly shows an individual α-Ag$_2$WO$_4$ crystal, which is uniform and dense. Moreover, the points highlighted in different colors on different crystal faces are related to the respective crystallographic planes. Fig. 5(b) illustrates this single α-Ag$_2$WO$_4$ crystal with the crystallographic planes (001), (00$\bar{1}$), (101), ($\bar{1}$0$\bar{1}$), ($\bar{1}$01), (10$\bar{1}$), (010), and (0$\bar{1}$0) for the 8 faces, which were modeled computationally using the crystal morphology editor/viewer (KrystalShaper) program (version 1.3.0 for Windows)[72] using the lattice parameters and atomic positions obtained from the Rietveld refinement data presented in Table 1a–d (for more details, see the ESI‡ (Fig. S1a, b)). In Fig. 5(c) and the dashed black squares in inset of Fig. 5(c), we note the appearance of an α-Ag$_2$WO$_4$ crystal with 12 faces owing to the increase in the MH processing temperature and highlight two of the new faces in violet. In addition, we verified a decrease in the average height and a slight increase in the average width distribution of α-Ag$_2$WO$_4$ crystals, which can result from the reduction of the average area of the (010) and (0$\bar{1}$0) planes owing to the appearance of four new faces related to the (0$\bar{1}$1), (0$\bar{1}\bar{1}$), (011), and (01$\bar{1}$) planes. Fig. 5(d) illustrates this single α-Ag$_2$WO$_4$ crystal with 12 faces, and more details of different perspectives can be found in the ESI‡ (Fig. S1c and d). As observed in Fig. 5(e) and the inset of Fig. 5(e), a slight decrease in the average height and an increase in the average width distribution of α-Ag$_2$WO$_4$ crystals were promoted by the increased MH processing temperature. This behavior can be related to the slight change in the lattice parameter, which promoted an increase in the width of α-Ag$_2$WO$_4$ crystals on the x-axis along the [100] direction and consequently decreased the area of the (010) and (0$\bar{1}$0) faces. This single α-Ag$_2$WO$_4$ crystal with 12 faces was modeled, as shown in Fig. 5(f), and more details of different perspectives can be found in the ESI‡ (Fig. S1e and f). Fig. 5(g) shows that some of the α-Ag$_2$WO$_4$ crystals with 14 faces grew further with an increase in the MH processing temperature. These new α-Ag$_2$WO$_4$ crystals are composed of 14 faces, where the four new faces of the lozenge-shaped crystal are ascribed to the (110), ($\bar{1}$10), ($\bar{1}\bar{1}$0) and (1$\bar{1}$0) crystallographic planes, and are shown as dashed black squares in insets of Fig. 5g and h. We propose the emergence of these four new faces in the α-Ag$_2$WO$_4$ crystals promoted the disappearance of the two faces related to (010) and (0$\bar{1}$0) planes to maintain the thermal and structural equilibrium of the orthorhombic lattice owing to the changes in the lattice parameters (Table 1a–d).

3.6. Growth mechanism, computational modeling, and surface energy analyses

Fig. 6a–c show the single α-Ag$_2$WO$_4$ crystals modeled computationally using the Rietveld refinement data and FE-SEM images. A Wulff construction was used to model optimized
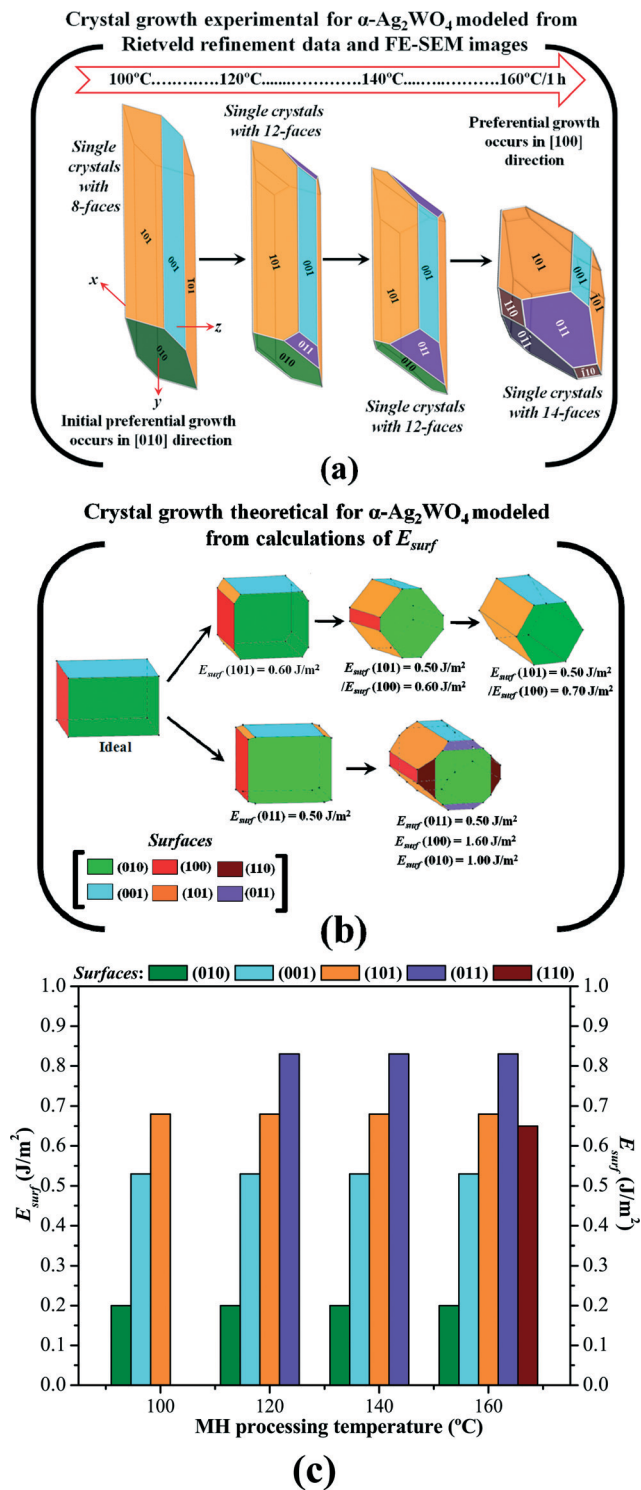
(a)

Crystal growth experimental for α-Ag₂WO₄ modeled from Rietveld refinement data and FE-SEM images

100°C.............120°C.......................140°C.....................160°C/1 h

Single crystals with 8-faces

Single crystals with 12-faces

Preferential growth occurs in [100] direction

Initial preferential growth occurs in [010] direction

Single crystals with 12-faces

Single crystals with 14-faces

(a)

(b)

Crystal growth theoretical for α-Ag₂WO₄ modeled from calculations of E_{surf}

Ideal

E_{surf} (101) = 0.60 J/m²

E_{surf} (101) = 0.50 J/m² /E_{surf} (100) = 0.60 J/m²

E_{surf} (101) = 0.50 J/m² /E_{surf} (100) = 0.70 J/m²

E_{surf} (011) = 0.50 J/m²

E_{surf} (011) = 0.50 J/m² E_{surf} (100) = 1.60 J/m² E_{surf} (010) = 1.00 J/m²

Surfaces

(010) (100) (110) (001) (101) (011)

(b)

(c)

(c)

Fig. 6 (a) Crystal shape simulated computationally for α-Ag₂WO₄ microcrystals synthesized by the MH method at different temperatures, (b) theoretical crystal shape for α-Ag₂WO₄ microcrystals using DFT calculations, (c) correlation between surface energy and MH processing temperature.

α-Ag₂WO₄ crystals with different shapes assuming different surface energy ratios obtained from the optimized surface energies (J m⁻²) of the different crystallographic planes.

Initially, before the growth and formation of large single α-Ag₂WO₄ crystals with 8 faces, initial nanocrystals related to the clusters arise, which correspond to the smallest nuclei and are directly related to the orthorhombic unit cell. This ideal α-Ag₂WO₄ crystal, if chemically prepared and controlled in the reaction medium, would have a size of approximately 1.2 nm in Table 1a–d. However, it is very difficult to control the crystal growth process (solids immersed in liquid) or the formation of crystals precipitated from solution.[73] Therefore, the formation of crystals with different shapes and sizes depends on the average concentration of the solution (unsaturated, saturated, or supersaturated).[74] In general, nanocrystals can be formed from unsaturated solutions in colloidal systems. Clusters are formed in a solution that is saturated at equilibrium.[73,74] The nucleation process occurs when crystals precipitate in a saturated solution, and the formation and accumulation of stable nuclei[75] occur when super-saturation is sufficiently high to overcome the nucleation energy barrier. In supersaturated solutions, crystal precipitates are already formed at the completion of the nucleation. In our system, the crystals continued to grow, and Fig. 6(a) shows the single α-Ag₂WO₄ crystals with 8 faces, 12 faces, or 14 faces obtained using MH processing at different temperatures for 1 h using 1 g of SDS. However, before the formation of these crystals, stoichiometric amounts of Ag⁺ ions were added to an aqueous solution of SDS. Anionic surfactants can facilitate the formation of micelles in H₂O when the critical micelle concentration is reached. This stage promotes interaction of the Ag⁺ ions with the interior of the negative micelles through electrostatic attraction to the negative polar head groups R–O–SO₃⁻ present in SDS as an anionic surfactant in the hydrophobic short chain (apolar) connected to a negative ionic group (head-polar).[75,76] These negative heads have more ability to bond with the Ag⁺ ions than with the WO₄²⁻ ions which are solvated by surrounding H₂O molecules.[77,78] However, the short-chain organic of SDS surfactant do not is strong sufficient to avoid the strong Coulombic electrostatic attraction between the 2Ag⁺ and 1WO₄²⁻ ions with those of during the MH processing, which results in the formation of the first α-Ag₂WO₄ precipitates or nucleation seeds. In sequence, these suspensions were transferred to a Teflon-lined autoclave, which was placed inside a domestic MH system. This apparatus was developed by several modifications of a microwave oven.[79,80] In this system, the high microwave frequency interacts with the permanent dipoles of the liquid phase (H₂O), initiating rapid heating via molecular rotation. Likewise, the permanent or induced dipoles in the dispersed phase promote rapid heating of the crystals.[81,82] The microwave radiation also promotes an increase in the effective collision rate between the particles in suspension, contributing to the crystal attachment and growth processes.[83] The adsorption of H₂O and SDS on the α-Ag₂WO₄ crystal surfaces favors aggregation and diffusion of the nanocrystals, leading to the fast growth of microcrystals, which adhere through van der Waals forces.[84] The evolution of the growth process to form the different α-Ag₂WO₄ crystals with 8, 12, and

14 faces is shown in Fig. 6(a). Moreover, in this work, we proposed that our α-Ag$_2$WO$_4$ crystals with 8 faces grow preferentially in the [010] direction along the y-axis. Finally, by heating the aqueous medium, the microwave radiation is able to promote crystal growth with new faces at high energy surfaces. This mechanism is probably one of the key factors responsible for the appearance of four new faces (((110), ($\bar{1}$10), ($\bar{1}\bar{1}$0), and (1$\bar{1}$0)) in the lozenge-shaped α-Ag$_2$WO$_4$ crystals, leading to preferential growth in the [100] direction along the x-axis. Fig. 6(b) illustrates the crystal growth using the Wulff construction to optimize α-Ag$_2$WO$_4$ and some shapes of α-Ag$_2$WO$_4$ crystals obtained assuming different surface energy ratios. Moreover, we have calculated the surface energy required for an ideal crystal to generate a prism shape. The ratio of the surface energy and optical band gap varied, with an increased value for the more stable surfaces (left) and a decreased value for the less stable surfaces (right). The *ab initio* calculated surface energy values for different crystalline planes are listed in Fig. S2(a)‡ along with the results of the Wulff constructions derived from the theoretical results. The theoretical shape of the α-Ag$_2$WO$_4$ crystals under equilibrium conditions was found to be hexagonal. A comparison between the shapes with 8 faces obtained experimentally at 100 °C and those modeled theoretically indicated that the theoretical shape shows minor elongation along the [010] direction. However, it was not possible to obtain a theoretical α-Ag$_2$WO$_4$ crystal with 14 faces similar to that obtained at 160 °C. Despite some differences between the vacuum conditions employed in the calculations and the actual conditions used for crystal growth, the most stable predicted faces usually showed the largest fraction of crystal surfaces.[53,85] Moreover, the surface energy values (J m^{-2}) of each face in the ideal α-Ag$_2$WO$_4$ crystals indicated that the (011) face has a high energy surface (E_{surf} = 0.83 J m^{-2}), as can be seen in Fig. 6(c). According to our theoretical surface energy results, the experimental α-Ag$_2$WO$_4$ crystals with 14 faces have more energetically active crystallographic planes than the other crystals.

In addition, the theoretical values for optical band gaps (E_{gap}) of each crystal surface are presented in Table 2.

This table indicates the effect of E_{gap} values at each surface of α-Ag$_2$WO$_4$ microcrystals and their respectives area and surface energies. In passing from 8-faceted crystal

to 14-faceted crystal, the optical band gap shows a slight variation from 3.09 to 3.16 eV at the same time that surface (010) disappears (with high computed E_{gap} value). Then, (110) and (011) surfaces gain importance, whose E_{gap} values compensate that of the (010) surface.

3.7. Photocatalytic activity of α-Ag$_2$WO$_4$ microcrystals for the degradation of RhB and Rh6G dyes

Fig. 7a–h show the PC degradation of RhB and Rh6G dyes by α-Ag$_2$WO$_4$ microcrystals monitored by the temporal changes in the UV–vis absorbance spectra of the aqueous dye solutions. Insets show digital photos of Rh6G aqueous dye solutions after different exposure times to UV light in the presence of the catalyst. The degradation rates (C_n/C_0) of the RhB and Rh6G aqueous dye solutions with different catalysts and without a catalyst are shown in Fig. 7i and j, and the rate constants (k) obtained for degradation of the RhB and Rh6G aqueous dye solutions are illustrated in Fig. 7l and k.

Fig. 7(a) indicates a significant reduction of around 80% at the maximum of the absorption spectra of the RhB aqueous solutions after 120 min of photodegradation with catalyst α-Ag$_2$WO$_4$ microcrystals prepared at 100 °C by the MH method. Before irradiation, the RhB dye, which is an N,N,N',N'-tetraethylated Rhodamine molecule, has one band with a maximum absorption centered at 554 nm. The photodecoloration of the RhB dye occurs because of an oxidative attack by an active oxygen species on a N-ethyl group.[86] We did not notice any shift in the maximum absorption of RhB dye to other wavelength positions of its major absorption band, which moved toward the N,N,N'-tri-ethylated Rhodamine (λ_{max} = 539 nm), N,N'-di-ethylated Rhodamine (λ_{max} = 522 nm), N-ethylated Rhodamine (λ_{max} = 510 nm), and Rhodamine (λ_{max} = 498 nm) species.[87] We assumed that a high percentage of RhB was destroyed or photodegraded after 120 min under UV light (see Fig. 7b–d). Moreover, we verified that our α-Ag$_2$WO$_4$ microcrystal catalyst obtained at 160 °C was the most efficient for the degradation of RhB under UV light owing to the presence of the high energy surface (E_{surf} = 0.83 J m^{-2}) of the (110) plane. These new results and important observations have not been previously reported in the literature on pure α-Ag$_2$WO$_4$ crystals as catalysts for the photodegradation of organic dyes.[7–9,19,20]

We also tested our α-Ag$_2$WO$_4$ microcrystals for the degradation of Rh6G. The Rh6G dye has one absorption band with a maximum centered at 526 nm. The results obtained indicated that the degradation of Rh6G as a function of UV-irradiation time with our crystals is more efficient than that of RhB (Fig. 7b–d and inset). We believe that this behavior is due to the better capability of the α-Ag$_2$WO$_4$ crystals to act as active sites for the Rh6G dyes. According to the literature,[88–90] the main factor responsible for the high efficiency photocatalysis with catalyst crystals is a low recombination rate between photogenerated electrons and holes on the crystal surface. Therefore, the holes (h$^{\bullet}$) generated by the distorted octahedral [WO$_6$]$_d^x$, deltahedral [AgO$_7$]$_d^x$, octahedral [AgO$_6$]$_d^x$,

Table 2 The number of Ag$_2$WO$_4$ units, area, surface energy and band gaps for (010), (001), (100), (101), (110) and (011) surfaces of α-Ag$_2$WO$_4$ crystals. The (010), (100), (101) and (011) surfaces are O and Ag-terminated; (001), (110) surfaces are O, W, and Ag-terminated

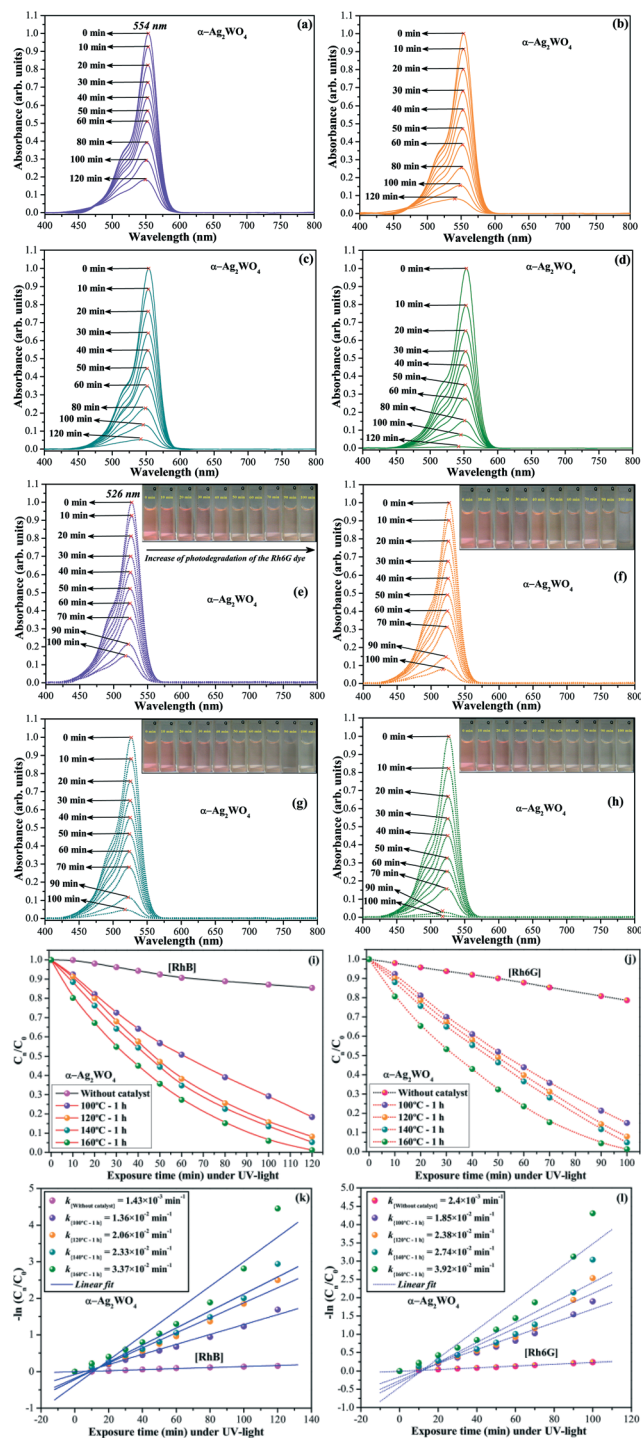| Surfaces	n	Area (Å^2)	E_{surf} (J m^{-2})	E_{gap} (eV)
(010)	8	64.1	0.20	1.39
(001)	16	132.5	0.53	0.65
(100)	8	68.6	0.38	0.48
(101)	9	149.2	0.68	1.15
(110)	10	93.9	0.65	1.05
(011)	16	147.2	0.83	0.55

Fig. 7 (a–h) Evolution of UV–vis absorption spectra after 120 min and 100 min of illumination for the photodegradation of RhB and Rh6G dyes by the α-Ag₂WO₄ microcrystals. The inset shows digital photos of photodegradation for the Rh6G after different illumination times with the UV lamps, (i and j) kinetics of weight-based photocatalytic degradation of RhB and Rh6G dyes by the catalysts and (k and l) first-order kinetics without and with catalysts.

tetrahedral $[AgO_4]_d^x$, and angular $[AgO_2]_d^x$ clusters affect the rate of recombination of the electron–hole pair.

Fig. 7i and j show that the RhB and Rh6G dyes were completely degraded after 120 and 100 min under UV light,

respectively. The photocatalytic degradation of Rh6G and RhB dyes by our α-Ag₂WO₄ crystal catalysts will be explained using the results obtained in chemical kinetics by the exponential decay curve (C_n/C_0). A photocatalytic test was conducted to show the efficiency differences of our α-Ag₂WO₄ crystals with 8, 12, and 14 faces. To quantitatively understand the reaction kinetics for the degradation of the RhB and Rh6G dyes by the catalyst crystals, as illustrated in Fig. 7(i, j), we applied the pseudo-first order model expressed in eqn (8) to obtain the rate constants (k):[91,92]

$$-\ln\left(\frac{C_n}{C_0}\right) = kt \tag{8}$$

where C_0 is the initial concentration (0 min) of the aqueous dye solution and C_n is the concentration of the aqueous dye solution at different times (min; n = 10, 20, 30…) of UV-light irradiation, t is the time, and k is the pseudo-first order rate constant. This equation is generally used for a photocatalytic degradation process if the initial concentration of the pollutant is low (1×10^{-5} mol L^{-1}).[92] According to eqn (8), a plot of $[-\ln(C_n/C_0)]$ as a function of t gives a straight line with slope k. All the results shown in Fig. 7k and l are absolute and were not normalized for the specific surface area (S_{BET}) of each crystal.[93] From Fig. 7k and l, the rate constants in the absence of a catalyst are very small ($k_{without\ catalyst} = 1.42 \times 10^{-3}$ min^{-1} for RhB and 2.39×10^{-3} min^{-1} for Rh6G), which indicate that there is no significant degradation of the RhB and Rh6G dyes after 120 and 100 min, respectively. Moreover, the rate constants for the degradation of RhB ($k_{\{100\ °C–1\ h\}} = 1.35 \times 10^{-2}$ min^{-1}, $k_{\{120\ °C–1\ h\}} = 2.05 \times 10^{-2}$ min^{-1}, $k_{\{140\ °C–1\ h\}} = 2.33 \times 10^{-2}$ min^{-1}, and $k_{\{160\ °C–1\ h\}} = 3.37 \times 10^{-2}$ min^{-1}) and Rh6G ($k_{\{100\ °C–1\ h\}} = 1.84 \times 10^{-2}$ min^{-1}, $k_{\{120\ °C–1\ h\}} = 2.37 \times 10^{-2}$ min^{-1}, $k_{\{140\ °C–1\ h\}} = 2.73 \times 10^{-2}$ min^{-1}, and $k_{\{160\ °C–1\ h\}} = 3.91 \times 10^{-2}$ min^{-1}) with the α-Ag₂WO₄ microcrystals are shown in these figures. Good correlation coefficients ($R \geq 0.96$) and standard deviations (SD ≤ 0.003) were obtained for all the results, which showed high degradation rates and a short half-life of up to 50 min. The standard of the kinetic constant normalized values for α-Ag₂WO₄ microcrystals are presented in Table 3.

The results obtained after the normalization of the kinetic parameters ($k_{\{absolute\}}$ and $k_{[normalized]}$) of the catalyst crystals for PC degradation of RhB and Rh6G aqueous dye solutions and S_{BET} are presented in Table 3 which shows that $k_{[normalized]}$ values are smaller than $k_{[absolute]}$ values, i.e., each catalyst crystal has a specific surface area (S_{BET}).[93] Therefore, it is necessary to normalize the $k_{\{absolute\}}$ values obtained. These $k_{[normalized]}$ values were obtained by dividing the $k_{\{absolute\}}$ values by the specific surface area (S_{BET}) of each catalyst and are presented in Table 3. After normalization, the rate constants of the catalyst crystals obey the following ascending order:

$$k_{[α\text{-}Ag_2WO_4–Rh6G–160\ °C–1\ h]} > k_{[α\text{-}Ag_2WO_4–RhB–160\ °C–1\ h]} > k_{[wc\text{-}Rh6G]} > k_{[wc\text{-}RhB]}.$$

After comparing several relationships between $k(k_{[Rh6G]}/k_{[RhB]})$ values of catalyst α-Ag₂WO₄ crystals obtained at 160 °C, we

Table 3 Absolute kinetic constants ($k_{\{absolute\}}$), normalized kinetic constants ($k_{[normalized]}$) and specific surface areas (S_{BET}) for the different catalyst α-Ag$_2$WO$_4$ crystals

Samples	$k_{\{absolute\}}$ (min^{-1})	S_{BET} (m^2 g^{-1})	$k_{[normalized]}$ (min^{-1} m^{-2} g^1)
wc-RhB	1.43×10^{-3}	—	—
wc-Rh6G	2.4×10^{-3}	—	—
α-Ag$_2$WO$_4$–100 °C–1 h–RhB	1.36×10^{-2}	4.05	3.36×10^{-3}
α-Ag$_2$WO$_4$–120 °C–1 h–RhB	2.06×10^{-2}	3.12	6.6×10^{-3}
α-Ag$_2$WO$_4$–140 °C–1 h–RhB	2.33×10^{-2}	2.76	8.45×10^{-3}
α-Ag$_2$WO$_4$–160 °C–1 h–RhB	3.37×10^{-2}	1.98	1.71×10^{-2}
α-Ag$_2$WO$_4$–100 °C–1 h–Rh6G	1.85×10^{-2}	4.05	4.57×10^{-3}
α-Ag$_2$WO$_4$–120 °C–1 h–Rh6G	2.38×10^{-2}	3.12	7.62×10^{-3}
α-Ag$_2$WO$_4$–140 °C–1 h–Rh6G	2.74×10^{-2}	2.76	9.92×10^{-3}
α-Ag$_2$WO$_4$–160 °C–1 h–Rh6G	3.92×10^{-2}	1.98	1.98×10^{-2}

wc-RhB and wc-Rh6G = dyes without catalyst, α-Ag$_2$WO$_4$ microcrystals obtained at different temperatures used as a catalyst for the degradation of RhB and Rh6G dyes.

observed that the normalized $k_{[Rh6G]}$ is approximately 2.2 times higher than the normalized $k_{[RhB]}$. Moreover, $k_{[\alpha\text{-}Ag_2WO_4\text{–}Rh6G\text{–}160\ °C\text{–}1\ h]}$ is approximately 16.4 times higher than the normalized $k_{[wc\text{-}Rh6G]}$, and $k_{[\alpha\text{-}Ag_2WO_4\text{–}RhB\text{–}160\ °C\text{–}1\ h]}$ is approximately 23.7 times higher than the normalized $k_{[wc\text{-}RhB]}$.

3.8. A possible photocatalytic mechanism for the degradation of RhB and Rh6G dyes by α-Ag$_2$WO$_4$ microcrystals

Fig. 8a–e illustrate a schematic representation of the main stages involved in the photocatalytic mechanism by which

Fig. 8 Proposal of photocatalytic reaction mechanism for the degradation of the RhB and Rh6G dye solutions by the catalysts α-Ag$_2$WO$_4$ microcrystals. (a) Distortions/defects in the electronic structure promoting the formation of intermediate energy levels within the E_{gap} ($'$ = electrons) are electronic transference between clusters in VB and CB. (b) Reducing clusters in VB concede electrons to CB and oxidizing clusters received electrons from CB and transference to O$_2$ and H$_2$O adsorbed in α-Ag$_2$WO$_4$ microcrystals by reducing clusters to degradation of the RhB/Rh6G dyes, (c) defects on the crystal surface exhibit a particular surface energy, which acts as a catalytic active site, (d) RhB*/Rh6G* dyes are susceptible to attack of highly oxidizing species and (e) after several cycles of photooxidation the degradation of RhB*/Rh6G* dyes by the formed oxidant radicals occurs.

α-Ag$_2$WO$_4$ crystals with an optical band gap (intermediary electronic levels/surface energy) generate oxidizing radicals for the degradation of RhB and Rh6G dyes in aqueous solution under UV light.

In our photocatalytic test, the initial stage is extremely important for the optimization of this process with heterogeneous photocatalysis, which is a very efficient technique for the degradation of organic pollutants, such as RhB and Rh6G dyes. In this process, it is necessary to have an optimal dispersion of crystals and dyes in the system before irradiation. We assume that this step is of fundamental importance for the reproducibility of these results and that the system reaches adsorption–desorption equilibrium. In the second stage, this well-dispersed system was stirred for 5 min inside a dark box followed by collection of the first 3 mL aliquot. Then, six UV lights were triggered to start the photocatalysis.

In our model, the ideal catalyst crystal should have some specific features and the most important events occur before excitation, *i.e.*, before irradiation with UV light (λ = 254 nm or $hv \approx 4.88$ eV) as shown in Fig. 8(a). As noted in previous analyses, our α-Ag$_2$WO$_4$ crystals obtained by the MH method have (order–disorder) structural defects ascribed to different types of distorted clusters ([WO$_6$]$_d$, [AgO$_7$]$_d$, [AgO$_6$]$_d$, [AgO$_4$]$_d$, and [AgO$_2$]$_d$) and ordered clusters ([WO$_6$]$_o$, [AgO$_7$]$_o$, [AgO$_6$]$_o$, [AgO$_4$]$_o$, and [AgO$_2$]$_o$). In addition, we have observed that other characteristics are also very important for improving PC activity in different semiconductor crystals, such as crystallographic preferred orientation, intermediary electronic levels, high surface energy, roughness, defects, high active surface area, facets and adsorption–desorption equilibrium.[21,22,94–98] According to the literature,[99] the main factor responsible for the high efficiency photocatalysis of the catalyst crystals is the low recombination rate between photogenerated electrons ($'$) and holes ($\cdot$) on the semiconductor surface. Our α-Ag$_2$WO$_4$ semiconductor catalyst already has the ability to generate the $' \leftrightarrow \cdot$ pairs. This characteristic is due to intrinsic defects in the lattice of semiconductor materials with intermediary levels between the VB and the CB, as shown in Fig. 8(a). Therefore, the presence of α-Ag$_2$WO$_4$ crystals with different intermediary electronic levels and consequently optical band gaps from E_{gap} = 3.09
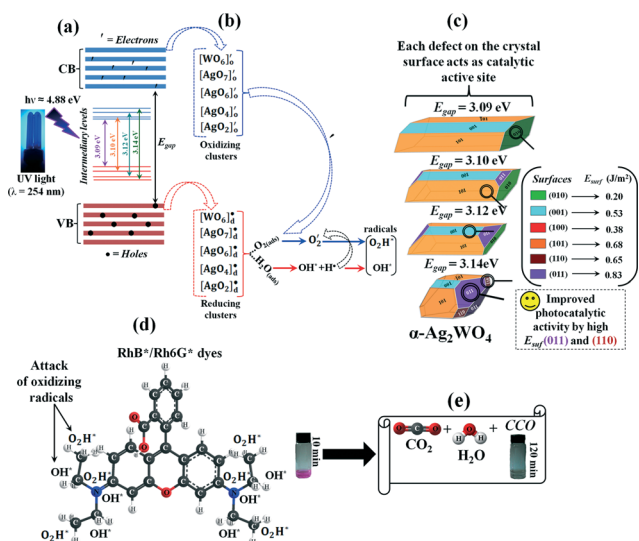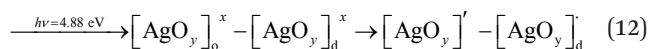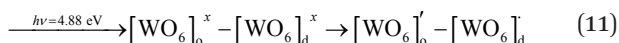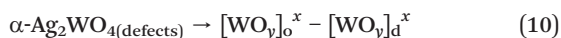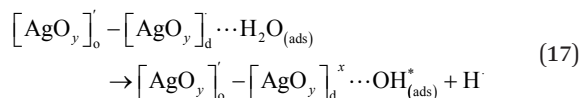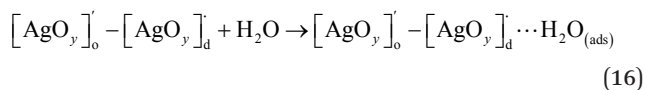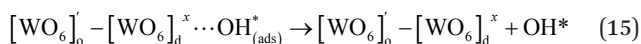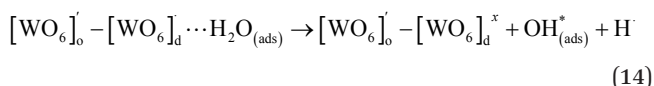
to 3.14 eV is due to specific structural defects, as well as different surface energies. These superficial/structural defects, which are caused by distorted $[WO_6]_d/[AgO_y]_d$ (y = 7, 6, 4, and 2) clusters, can polarize the lattice and lead to possible electronic transitions between disordered/distorted $[WO_6]_d{}^x/[AgO_y]_d{}^x$ and ordered $[WO_6]_o{}^x/[AgO_y]_o{}^x$ clusters. When UV light is absorbed by the α-Ag₂WO₄ crystals, the following processes can occur, as expressed in eqn (9)–(12) below:

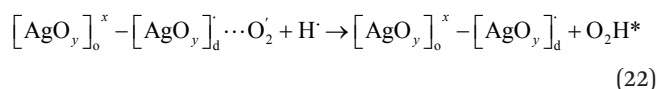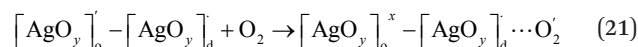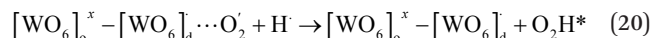$$\alpha\text{-Ag}_2\text{WO}_{4(\text{defects})} \rightarrow [WO_6]_o{}^x - [WO_6]_d{}^x \quad (9)$$

$$\alpha\text{-Ag}_2\text{WO}_{4(\text{defects})} \rightarrow [WO_y]_o{}^x - [WO_y]_d{}^x \quad (10)$$

$$\xrightarrow{h\nu=4.88\text{ eV}} [WO_6]_o{}^x - [WO_6]_d{}^x \rightarrow [WO_6]_o' - [WO_6]_d^{\cdot} \quad (11)$$

$$\xrightarrow{h\nu=4.88\text{ eV}} [AgO_y]_o{}^x - [AgO_y]_d{}^x \rightarrow [AgO_y]_o' - [AgO_y]_d^{\cdot} \quad (12)$$
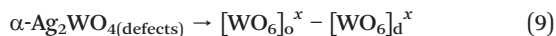
where y = 7, 6, 4, and 2.

As shown in Fig. 8a and b, we propose that the disordered/distorted $[WO_6]_d^{\cdot}$ and $[AgO_y]_d^{\cdot}$ clusters are located in intermediate levels near the VB, whereas the ordered $[WO_6]_o'$ and $[AgO_y]_o'$ clusters are located in intermediate levels below the CB. This process leads to the formation of $' \leftrightarrow \cdot$ pairs within the crystal band gap and also on the semiconductor surface. Thus, each specific defect on the semiconductor surface acts as a catalytic active site owing to different energy values on the surfaces, as shown in Fig. 8(c). During the photooxidation processes, the reducing $[WO_6]_d^{\cdot}$ and $[AgO_y]_d^{\cdot}$ clusters near the VB and located on the crystal surface can interact with H₂O and O₂ molecules present in the solution by means of adsorption (ads) processes as shown in Fig. 8(b) and eqn (13)–(18):

$$[WO_6]_o' - [WO_6]_d^{\cdot} + H_2O \rightarrow [WO_6]_o' - [WO_6]_d^{\cdot} \cdots H_2O_{(ads)} \quad (13)$$

$$[WO_6]_o' - [WO_6]_d^{\cdot} \cdots H_2O_{(ads)} \rightarrow [WO_6]_o' - [WO_6]_d{}^x + OH^*_{(ads)} + H^{\cdot} \quad (14)$$

$$[WO_6]_o' - [WO_6]_d{}^x \cdots OH^*_{(ads)} \rightarrow [WO_6]_o' - [WO_6]_d{}^x + OH^* \quad (15)$$

$$[AgO_y]_o' - [AgO_y]_d^{\cdot} + H_2O \rightarrow [AgO_y]_o' - [AgO_y]_d^{\cdot} \cdots H_2O_{(ads)} \quad (16)$$

$$[AgO_y]_o' - [AgO_y]_d^{\cdot} \cdots H_2O_{(ads)} \rightarrow [AgO_y]_o' - [AgO_y]_d{}^x \cdots OH^*_{(ads)} + H^{\cdot} \quad (17)$$

$$[AgO_y]_o{}^x - [AgO_y]_d^{\cdot} \cdots OH^*_{(ads)} \rightarrow [AgO_y]_o' - [AgO_y]_d{}^x + OH^* \quad (18)$$
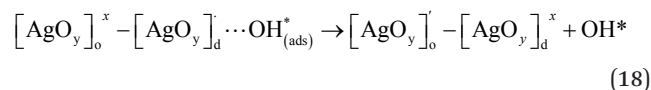
where y = 7, 6, 4, and 2.
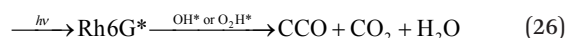
In the CB, the oxidizing $[WO_6]_o'$ and $[AgO_y]_o'$ clusters located on the semiconductor surface are able to react with the O₂(ads) molecules by means of electron transference. However, before this process, the H⁺ species (eqn (14) and (17)) are able to interact with the superoxide radical anion (O₂') forming the perhydroxyl radical (O₂H*) as shown in Fig. 8(b) and eqn (19)–(22):

$$[WO_6]_o' - [WO_6]_d^{\cdot} + O_2 \rightarrow [WO_6]_o{}^x - [WO_6]_d^{\cdot} \cdots O_2' \quad (19)$$

$$[WO_6]_o{}^x - [WO_6]_d^{\cdot} \cdots O_2' + H^{\cdot} \rightarrow [WO_6]_o{}^x - [WO_6]_d^{\cdot} + O_2H^* \quad (20)$$

$$[AgO_y]_o' - [AgO_y]_d^{\cdot} + O_2 \rightarrow [AgO_y]_o{}^x - [AgO_y]_d^{\cdot} \cdots O_2' \quad (21)$$

$$[AgO_y]_o{}^x - [AgO_y]_d^{\cdot} \cdots O_2' + H^{\cdot} \rightarrow [AgO_y]_o{}^x - [AgO_y]_d^{\cdot} + O_2H^* \quad (22)$$

Moreover, the RhB and Rh6G dyes are also excited by UV light, as shown in Fig. 8(d) and eqn (23) and (24):

$$\xrightarrow{h\nu} RhB \rightarrow RhB^* \quad (23)$$

$$\xrightarrow{h\nu} Rh6G \rightarrow Rh6G^* \quad (24)$$

These cycles occur continuously while the system is exposed to UV light. Finally, after several cycles (120 and 100 min) of photooxidation, the degradation of RhB* and Rh6G* by OH* and O₂H* radicals occurs, as shown in Fig. 8d and e and indicated by eqn (25) and (26):

$$\xrightarrow{h\nu} RhB^* \xrightarrow{OH^* \text{ or } O_2H^*} CCO + CO_2 + H_2O \quad (25)$$

$$\xrightarrow{h\nu} Rh6G^* \xrightarrow{OH^* \text{ or } O_2H^*} CCO + CO_2 + H_2O \quad (26)$$

where CCO = colorless compounds organic.[94]

Based on this photocatalytic mechanism, we assume that the defects on the crystal surface and the electronic structure of the distorted/disordered $[WO_6]_d^{\cdot}$ and $[AgO_y]_d^{\cdot}$ clusters and ordered $[WO_6]_o'$ and $[AgO_y]_o'$ clusters play an important role in the production of OH* and O₂H* radicals, which are the most oxidizing species in these chemical reactions for the degradation of the organic RhB and Rh6G dyes in aqueous solution.
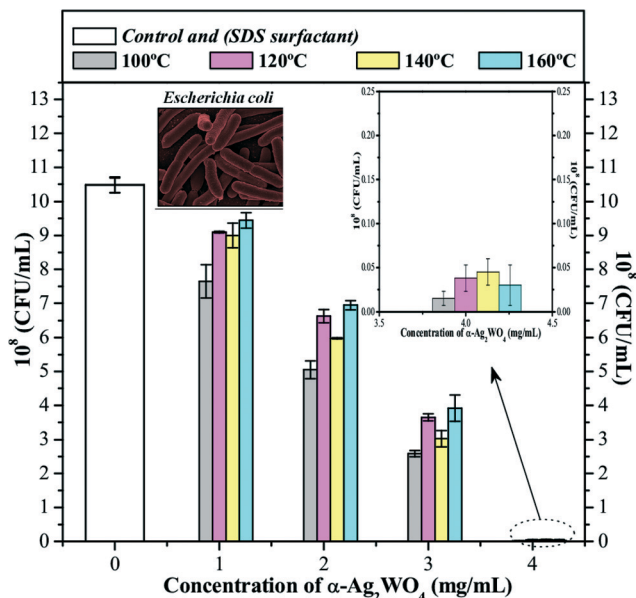
Fig. 9 Rate of inactivation for *E. coli* bacteria as a function of different concentrations of α-Ag$_2$WO$_4$ catalyst crystals.

3.9. Evaluation of antibacterial activity of crystals

Fig. 9 shows the inactivation of *E. coli* at different concentrations of the α-Ag$_2$WO$_4$ catalyst crystals.

The progressive antibacterial effects of our α-Ag$_2$WO$_4$ catalyst crystals for the inhibition of 1.5×10^8 CFU mL^{-1} *E. coli* as function of concentration (mg L^{-1}) are illustrated in Fig. 9. An analysis of the results indicates that at all concentrations of the α-Ag$_2$WO$_4$ crystals obtained at 100 °C have a higher efficiency of inactivation of *E. coli* bacteria. As previously shown in the FE-SEM images and simulated single crystals (Fig. 5a, b), these crystals do not have (0$\bar{1}$1), (0$\bar{1}\bar{1}$), (011), (01$\bar{1}$), (110), ($\bar{1}$10), ($\bar{1}\bar{1}$0), and (1$\bar{1}$0) planes and faces. Therefore, based on our experimental observations and theoretical calculations, we propose that the α-Ag$_2$WO$_4$ crystals with exposed (010) and (0$\bar{1}$0) faces and low surface energy ($E_{surf} = 0.20$ J m^{-2}) are more efficient for the inactivation of *E. coli* bacteria than the other crystals, as shown in Fig. 6(c) and 9. An explanation of this inactivation or destruction of *E. coli* bacteria is related to the presence of specific defects on the crystal surface and uncoordinated [AgO$_{y-z}$]$_d$ (y = 7, 6, 4, and 2 and z = 3, 2 and 1) clusters (see ESI‡ (Fig. S2a–d)), which also produce OH* and O$_2$H* radicals under visible light, although in low concentration, in aqueous solution.[100] These oxidizing radicals and crystal surfaces can interact with the main components of the bacterial cell, including the peptidoglycan cell wall, plasma membrane, cytoplasmic DNA, and bacterial proteins,[101–104] and can also induce the collapse of bacterial membranes.[105] Therefore, these results are similar to those recently reported in the literature[106,107] and are explained by eqn (19)–(22). Finally, we proposed the plausible mechanism of α-Ag$_2$WO$_4$ microcrystals to inactivation of *E. coli* bacteria involves the direct interaction between specific (010) and (0$\bar{1}$0) surfaces and cell surfaces, which affects the permeability of membranes where the low surface energy enters and induces oxidative stress in bacterial cells, subsequently resulting in the inhibition of cell growth and eventually in cell death.

4. Conclusions

In summary, the face-dependent photocatalytic and antibacterial properties of α-Ag$_2$WO$_4$ microcrystals were studied in detail by combining experimental techniques and first-principles calculations. Using this combined method, we clarified the important issues and established a theoretical base. Herein, we have systematically investigated, for first time, both the surface atomic and electronic structures of α-Ag$_2$WO$_4$ crystals with various exposed faces, which were prepared by the MH method using an anionic surfactant. The XRD patterns and Rietveld refinement data indicated that these crystals are monophasic with an orthorhombic structure. The structural refinement data were employed to model [AgO$_y$] (y = 7, 6, 4, and 2) and [WO$_6$] clusters. The UV–vis diffuse reflectance spectra indicated that the various α-Ag$_2$WO$_4$ microcrystals obtained using the MH method have different E_{gap} values, which suggest the presence of intermediate electronic levels between the VB and the CB. The shape and growth processes of these crystals can be modified using the anionic surfactant SDS and temperature. The predominant exposed facets varied from (010) and (0$\bar{1}$0) to (110) and (011), and facet-dependent photocatalytic activity for the degradation of RhB and Rh6G dyes indicated that the performance was dependent on the exposed crystal facets in the order (110) > (011) > (010) > (0$\bar{1}$0), which may be attributed to the different number of unsaturated superficial Ag and W sites capable of forming the main active adsorption sites for H$_2$O, O$_2$, OH*, and O$_2$H* radicals. The biological tests showed that the α-Ag$_2$WO$_4$ crystals with predominant (010) and (0$\bar{1}$0) surfaces with low surface energy had superior antibacterial activity for the inactivation of *E. coli* bacteria. These observations have broad implications for the growth mechanisms of a wide range of materials synthesized using different surfactants. The main message of this work is that different facets of α-Ag$_2$WO$_4$ crystals exhibit markedly different chemical and physical properties and that knowledge of their electronic properties allows for knowledge-led design of crystal morphologies to improve performance in various applications. By using this innovative and novel procedure, the presented model accurately describes the experimental results quantitatively and the atomic modeling explains these activities on the basis of the facets of the α-Ag$_2$WO$_4$ crystals. We have demonstrated a new approach to understand the role of the α-Ag$_2$WO$_4$ crystal surfaces, which also has great potential for addressing many fundamental issues in related materials. These insights can contribute to the rational design of new materials for multifunctional applications. Similar approaches to those described here could be employed to optimize the morphology of materials for a wide range of applications in solid-state lighting, solar cells, and

photocatalysis. Finally, we conclude this manuscript by quoting the observation that "New tools lead to new science",[108] which is perhaps nowhere more evident than in the present work. Following Dirac's statement,[109] "It therefore becomes desirable that approximate practical methods of applying quantum mechanics should be developed, which can lead to an explanation of the main features of complex atomic systems without too much computation". The present research can be considered a working example of the so-called "complex modeling paradigm", introduced by Billinge and Levin:[110] "We suggest that successful solutions to these nanostructure problems will involve interactions among researchers from materials science, physics, chemistry, computer science, and applied mathematics, working within a "complex modeling" paradigm that combines theory and experiment in a self-consistent computational framework".

Acknowledgements

Notes and references

1 L. S. Cavalcante, M. A. P. Almeida, W. Avansi Jr., R. L. Tranquilin, E. Longo, N. C. Batista, V. R. Mastelaro and M. Siu Li, *Inorg. Chem.*, 2012, **51**, 10675–10687.

2 E. Longo, L. S. Cavalcante, D. P. Volanti, A. F. Gouveia, V. M. Longo, J. A. Varela, M. O. Orlandi and J. Andrés, *Sci. Rep.*, 2013, **3**, 1676–1679.

3 J. Andrés, L. Gracia, P. Gonzalez-Navarrete, V. M. Longo, W. Avansi Jr., D. P. Volanti, M. M. Ferrer, P. S. Lemos, F. A. L. Porta, A. C. Hernandes and E. Longo, *Sci. Rep.*, 2014, **4**, 5391–5397.

4 E. Longo, D. P. Volanti, V. M. Longo, L. Gracia, I. C. Nogueira, M. A. P. Almeida, A. N. Pinheiro, M. M. Ferrer, L. S. Cavalcante and J. Andrés, *J. Phys. Chem. C*, 2014, **118**, 1229–1239.

5 W. S. Pereira, J. Andrés, L. Gracia, M. A. San-Miguel, E. Z. Silva, E. Longo and V. M. Longo, *Phys. Chem. Chem. Phys.*, 2015, **17**, 5352–5359.

6 Y. V. B. De Santana, L. Matos, G. Henrique, A. P. Cruvinel, C. Perrin, J. Andrés, J. A. Varela and E. Longo, *Nanomater. Nanotechnol.*, 2014, **4**, 22–31.

7 R. Zhang, H. Cui, X. Yang, H. Tang, H. Liu and Y. Li, *Micro Nano Lett.*, 2012, **7**, 1285–1288.

8 J. Zhu, H. Fan, J. Sun and S. Ai, *Sep. Purif. Technol.*, 2013, **120**, 134–140.

9 X. Liu, J. Hu, J. Li, Y. Hu, Y. Shao, H. Yang, G. Tong and H. Qian, *Mater. Lett.*, 2013, **91**, 129–132.

10 L. F. Silva, A. C. Catto, W. Avansi Jr., L. S. Cavalcante, J. Andrés, K. Aguir, V. R. Mastelaro and E. Longo, *Nanoscale*, 2014, **6**, 4058–4062.

11 D. P. Dutta, A. Singh, A. Ballal and A. K. Tyagi, *Eur. J. Inorg. Chem.*, 2014, **2014**, 5724–5732.

12 V. M. Longo, C. C. De Foggi, M. M. Ferrer, A. F. Gouveia, R. S. Andre, W. Avansi, C. E. Vergani, A. L. Machado, J. Andrés, L. S. Cavalcante, A. C. Hernandes and E. Longo, *J. Phys. Chem. A*, 2014, **118**, 5769–5778.

13 Q.-W. Song, B. Yu, X.-D. Li, R. Ma, Z. F. Diao, R.-G. Li, W. Li and L.-N. He, *Green Chem.*, 2014, **16**, 1633–1638.

14 C.-X. Guo, B. Yu, J.-N. Xie and L.-N. He, *Green Chem.*, 2015, **17**, 474–479.

15 L. Pan, L. Li and Y. Chen, *J. Sol-Gel Sci. Technol.*, 2013, **66**, 330–336.

16 S. Muthamizh, K. Giribabu, R. Suresh, R. Manigandan, S. Munusamy, S. P. Kumar and V. J. Narayanan, *Int. J. ChemTech Res.*, 2014, **6**, 392–3394.

17 V. P. Fadeeva, V. D. Tikhova, Y. M. Deryabina and O. N. Nikulicheva, *J. Struct. Chem.*, 2014, **55**, 972–979.

18 A. J. Vandenberg and C. A. H. Juffermans, *J. Appl. Crystallogr.*, 1982, **15**, 114–116.

19 H. Chen and Y. Xu, *Appl. Surf. Sci.*, 2014, **319**, 319–323.

20 X. Y. Zhang, J. D. Wang, J. K. Liu, X. H. Yang and Y. Lu, *CrystEngComm*, 2015, **17**, 1129–1138.

21 L. S. Cavalcante, J. C. Sczancoski, N. C. Batista, E. Longo, J. A. Varela and M. O. Orlandi, *Adv. Powder Technol.*, 2013, **24**, 344–353.

22 L. S. Cavalcante, F. M. C. Batista, M. A. P. Almeida, A. C. Rabelo, I. C. Nogueira, N. C. Batista, J. A. Varela, M. R. M. C. Santos, E. Longo and M. S. Li, *RSC Adv.*, 2012, **2**, 6438–6454.

23 M. Qamar and A. Khan, *RSC Adv.*, 2014, **4**, 9542–9550.

24 X. Wang, C. Fu, P. Wang, H. Yu and J. Yu, *Nanotechnology*, 2013, **24**, 165602–165609.

25 Q. P. Wang, X. X. Guo, W. H. Wu and S. X. Liu, *Adv. Mater. Res.*, 2011, **284–286**, 1321–1325.

26 Z. Li, A. J. Clarke and T. J. J. Beveridge, *J. Bacteriol.*, 1998, **180**, 5478–5483.

27 M. R. S. A. L. De Moura, M. J. G. De Mello, W. B. Calábria, E. M. Germano, R. R. S. Maggi and J. B. Correia, *Rev. Bras. Saude Prod. Anim.*, 2012, **12**, 173–182.

28 B. G. Trewyn, C. M. Whitman and V. S. Y. Lin, *Nano Lett.*, 2004, **4**, 2139–2143.

29 M. Thukkaram, S. Sitaram, S. K. Kannaiyan and G. Subbiahdoss, *Int. J. Biomater.*, 2014, **2014**, 716080–716085.

30 Z. X. Tang and B. F. Lv, *Braz. J. Chem. Eng.*, 2014, **31**, 591–601.

31 S. H. Hsu, H. J. Tseng and Y. C. Lin, *Biomaterials*, 2010, **31**, 6796–6808.

32 R. Prucek, J. Tucek, M. Kilianová, A. Panácek and K. Tománková, *Biomaterials*, 2011, **32**, 4704–4713.

33 L. Zhao, H. Wang, K. Huo, L. Cui, W. Zhang, H. Ni, Y. Zhang, Z. Wu and P. Chu, *Biomaterials*, 2011, **32**, 5706–5716.

34 S. Ifuku, M. Tsuji, M. Morimoto, H. Saimoto and H. Yano, *Biomacromolecules*, 2009, **10**, 2714–2717.

35 A. D. Russell and W. B. Hugo, *Prog. Med. Chem.*, 1994, **31**, 351–370.

36 V. Sambhy, M. M. MacBride, B. R. Peterson and A. Sen, *J. Am. Chem. Soc.*, 2006, **128**, 9798–9808.

37 K. H. Jang, Y. J. Yu, Y. H. Lee, Y. O. Kang and W. H. Park, *Mater. Lett.*, 2014, **116**, 146–149.

38 D. Chudobova, D. Maskova, L. Nejdl, P. Kopel, M. A. M. Rodrigo, V. Adam and R. Kizek, *Microbial pathogens and strategies for combating them: science, technology and education*, Formatex, 2013, vol. 3, pp. 728–735.

39 G. Kresse and J. Furthmuller, *Comput. Mater. Sci.*, 2007, **6**, 15–50.

40 G. Kresse and J. Furthmuller, *Phys. Rev. B: Condens. Matter Mater. Phys.*, 1996, **54**, 11169–11186.

41 G. Kresse and J. Hafner, *Phys. Rev. B: Condens. Matter Mater. Phys.*, 1993, **47**, 558–561.

42 J. P. Perdew, K. Burke and M. Ernzerhof, *Phys. Rev. Lett.*, 1996, **77**, 3865–3868.

43 J. P. Perdew, J. A. Chevary, S. H. Vosko, K. A. Jackson, M. R. Pederson, D. J. Singh and C. Fiolhais, *Phys. Rev. B: Condens. Matter Mater. Phys.*, 1992, **46**, 6671–6687.

44 P. E. Blochl, *Phys. Rev. B: Condens. Matter Mater. Phys.*, 1994, **50**, 17953–17979.

45 G. Kresse and D. Joubert, *Phys. Rev. B: Condens. Matter Mater. Phys.*, 1999, **59**, 1758–1775.

46 G. Wulff, *Z. Phys. Chem. (Muenchen, Ger.)*, 1901, **34**, 449–530.

47 A. Seyed-Razavi, I. K. Snook and A. S. Barnard, *J. Mater. Chem.*, 2010, **20**, 416–421.

48 M. A. Lovette, A. R. Browning, D. W. Griffin, J. P. Sizemore, R. C. Snyder and M. F. Doherty, *Ind. Eng. Chem. Res.*, 2008, **47**, 9812–9833.

49 J. Chen, B. Lim, E. P. Lee and Y. Xia, *Nano Today*, 2009, **4**, 81–95.

50 Z. Y. Jiang, Q. Kuang, Z. X. Xie and L. S. Zheng, *Adv. Funct. Mater.*, 2010, **20**, 3634–3645.

51 D. G. Stroppa, L. A. Montoro, A. Beltrán, T. G. Conti, R. O. Silva, J. Andrés, E. Longo, E. R. Leite and A. J. Ramirez, *J. Am. Chem. Soc.*, 2009, **131**, 14544–14548.

52 M. R. D. Bomio, R. L. Tranquilin, F. V. Motta, C. A. Paskocimas, R. M. Nascimento, L. Gracia, J. Andrés and E. Longo, *J. Phys. Chem. C*, 2013, **117**, 2138–21395.

53 V. M. Longo, L. Gracia, D. G. Stroppa, L. S. Cavalcante, M. Orlandi, A. J. Ramirez, E. R. Leite, J. Andrés, A. Beltrán, J. A. Varela and E. Longo, *J. Phys. Chem. C*, 2011, **115**, 20113–20119.

54 P. M. Skarstad and S. Geller, *Mater. Res. Bull.*, 1975, **10**, 791–800.

55 P. Wang, B. Huang, X. Qin, X. Zhang, Y. Dai and M. H. Whangbo, *Inorg. Chem.*, 2009, **48**, 10697–10702.

56 E. Tomaszewicz, H. Fuks, J. Typek, B. Sawicki, M. Oboz, T. Groń and T. Mydlarz, *Ceram. Int.*, 2015, **41**, 5734–5748.

57 H. M. Rietveld, *J. Appl. Crystallogr.*, 1969, **2**, 65–71.

58 A. C. Larson and R. B. Von Dreele, *General structure analysis system (GSAS)*, Los Alamos, National Laboratory, 2001, pp. 124–213.

59 A. R. Roosen, R. P. McCormack and W. C. Carter, *Comput. Mater. Sci.*, 1998, **11**, 16–26.

60 L. W. Finger, D. E. Cox and A. P. Jephcoat, *J. Appl. Crystallogr.*, 1994, **27**, 892–900.

61 P. W. Stephens, *J. Appl. Crystallogr.*, 1999, **32**, 281–289.

62 K. Momma and F. Izumi, *J. Appl. Crystallogr.*, 2008, **41**, 653–658.

63 K. Momma and F. Izumi, *J. Appl. Crystallogr.*, 2011, **44**, 1272–1276.

64 P. Kubelka and F. Munk, *Z. Fur Tech. Phys.*, 1931, **12**, 593–601.

65 M. L. Myrick, M. N. Simcock, M. Baranowski, H. Brooke, S. L. Morgan and J. N. Mccutcheon, *Appl. Spectrosc. Rev.*, 2011, **46**, 140–165.

66 R. A. Smith, *Semiconductors*, Cambridge University Press, London, 2nd edn, 1978, p. 434.

67 J. Tang and J. Ye, *J. Mater. Chem.*, 2005, **15**, 4246–4251.

68 D. W. Kim, I. S. Cho, S. Lee, S. T. Bae, S. S. Shin, G. S. Han, H. S. Jung and K. S. Hong, *J. Am. Ceram. Soc.*, 2010, **93**, 3867–3872.

69 A. S. Barnard and P. Zapol, *J. Chem. Phys.*, 2004, **121**, 4276–4283.

70 A. F. Gouveia, J. C. Sczancoski, M. M. Ferrer, A. S. Lima, M. R. M. C. Santos, M. S. Li, R. S. Santos, E. Longo and L. S. Cavalcante, *Inorg. Chem.*, 2014, **53**, 5589–5599.

71 S. Vidya, S. Solomon and J. K. Thomas, *Phys. Status Solidi A*, 2012, **6**, 1067–1074.

72 http://www.jcrystal.com/products/krystalshaper/.

73 J. Park, J. Joo, S. G. Kwon, Y. Jang and T. Hyeon, *Angew. Chem., Int. Ed.*, 2007, **46**, 4630–4660.

74 J. J. de Yoreo and P. Vekilov, Principles of crystal nucleation and growth, in *Biomineralization*, Mineralogical Society of America, Washington, DC, 2003, pp. 57–65.

75 L. S. Cavalcante, J. C. Sczancoski, M. S. Li, E. Longo and J. A. Varela, *Colloids Surf., A*, 2012, **396**, 346–351.

76 L. L. Gao, S. Y. Song, J. F. Ma and J. Yang, *J. Nanosci. Nanotechnol.*, 2013, **13**, 4228–4234.

77 L. F. Scatena and G. L. Richmond, *J. Phys. Chem. B*, 2004, **108**, 12518–12528.

78 X. Z. Li, B. Walker and A. Michaelides, *Proc. Natl. Acad. Sci. U. S. A.*, 2011, **108**, 6369–6373.

79 http://www.panasonic.com/br/consumidor/ eletrodomesticos/micro-ondas.html.

80 E. L. da Silva, J. A. Varela, D. K. A. Almeida and D. P. Volanti, Pat. Number(s): BR200815393-A2, Dec. 7, 2010.

81 G. J. Wilson, A. S. Matijasevich, D. R. G. Mitchell, J. C. Schulz and G. D. Will, *Langmuir*, 2006, **22**, 2016–2027.

82 G. J. Wilson, A. S. Matijasevich, D. R. G. Mitchell, J. C. Schulz and G. D. Will, *Langmuir*, 2006, **22**, 2016–2027.

83 M. Godinho, C. Ribeiro, E. Longo and E. R. Leite, *Cryst. Growth Des.*, 2008, **8**, 384–386.

84 A. P. Moura, L. S. Cavalcante, J. C. Sczancoski, D. G. Stroppa, E. C. Paris, A. J. Ramirez, J. A. Varela and E. Longo, *Adv. Powder Technol.*, 2010, **21**, 197–202.

85 G. Liu, J. C. Yu, G. Q. Lu and H. M. Cheng, *Chem. Commun.*, 2011, **47**, 6763–6783.

86 Y. Zhao, C. Li, X. Liu and F. Gu, *J. Alloys Compd.*, 2007, **440**, 281–286.

87 T. Wu, G. Liu, J. Zhao, H. Hidaka and N. Serpone, *J. Phys. Chem. B*, 1998, **102**, 5845–5851.

88 J. Li, C. Yu, C. Zheng, A. Etogo, Y. Xie, Y. Zhong and Y. Hu, *Mater. Res. Bull.*, 2015, **61**, 315–320.

89 A. R. Malagutti, H. A. J. L. Mourão, J. R. Garbin and C. Ribeiro, *Appl. Catal., B*, 2009, **205**, 205–212.

90 K. Yu, S. Yang, H. He, C. Sun, C. Gu and Y. Ju, *J. Phys. Chem. A*, 2006, **113**, 10024–10032.

91 J. Bi, L. Wu, Z. Li, Z. Ding, X. Wang and X. Fu, *J. Alloys Compd.*, 2009, **480**, 684–688.

92 Y. Zhao, C. Li, X. Liu and F. Gu, *J. Alloys Compd.*, 2007, **440**, 281–286.

93 S. Brunauer, P. H. Emmett and E. Teller, *J. Am. Chem. Soc.*, 1938, **60**, 309–319.

94 P. Li, X. Zhao, Y. Li, H. Sun, L. Sun, X. Cheng, X. Hao and W. Fan, *CrystEngComm*, 2012, **14**, 920–928.

95 M. Zhao, H. Xu, H. Chen, S. Ouyang, N. Umezawa, D. Wang and J. Ye, *J. Mater. Chem. A*, 2015, **3**, 2331–2337.

96 M. Huang, S. Weng, B. Wang, J. Hu, X. Fu and P. Liu, *J. Phys. Chem. C*, 2014, **118**, 25434–25440.

97 S. K. Wallace and K. P. Mckenna, *J. Phys. Chem. C*, 2015, **119**, 1913–1920.

98 Z. Wan and G. Zhang, *Sci. Rep.*, 2014, **4**, 6298–6306.

99 A. Zhang and J. Zhang, *J. Mater. Sci.*, 2010, **45**, 4040–4045.

100 K. Loza, J. Diendorf, C. Sengstock, L. Ruiz-Gonzalez, J. M. Gonzalez-Calbet, M. Vallet-Regi, M. Koller and M. Epple, *J. Mater. Chem. B*, 2014, **2**, 1634–1643.

101 G. J. Zhao and S. E. Stevens, *Biomaterials*, 1998, **11**, 27–32.

102 S. Ninganagouda, V. Rathod, D. Singh, J. Hiremath, A. K. Singh and J. Mathew, *BioMed Res. Int.*, 2014, **2014**, 753419–753428.

103 M. Yamanaka, K. Hara and J. Kudo, *Appl. Environ. Microbiol.*, 2005, **71**, 7589–7593.

104 W. K. Jung, H. C. Koo, K. W. Kim, S. Shin, S. H. Kim and Y. H. Park, *Appl. Environ. Microbiol.*, 2008, **74**, 2171–2178.

105 J. W. Xu, Z. D. Gao, K. Han, Y. Liu and Y. Y. Song, *ACS Appl. Mater. Interfaces*, 2014, **6**, 15122–15131.

106 V. Q. Nguyen, M. Ishihara, J. Kinoda, H. Hattori, S. Nakamura, T. Ono, Y. Miyahira and T. Matsui, *J. Nanobiotechnol.*, 2014, **12**, 49–58.

107 W. A. Ismail, Z. A. Ali and R. Puteh, *J. Nanomater.*, 2013, **2013**, 901452–901458.

108 P. S. Weiss, *ACS Nano*, 2012, **6**, 1877–1879.

109 P. A. M. Dirac, *Proc. R. Soc. London*, 1929, **123**, 714–733.

110 S. J. L. Billinge and I. Levin, *Science*, 2007, **316**, 561–565.